Spring 5-14-2021

Functional Importance of Non-Catalytic Residues in the Active Site of NADH:Quinone Oxidoreductase From Pseudomonas aeruginosa PA01

Benjamin Dratch
bdratch1@student.gsu.edu

Gioavanni Gadda
Georgia State University

Functional Importance of Non-Catalytic Residues in the Active Site of NADH:Quinone Oxidoreductase From *Pseudomonas aeruginosa* PA01

by

Benjamin Deen Dratch

Under the Direction of Giovanni Gadda, PhD

A Thesis Submitted in Partial Fulfillment of the Requirements for the Degree of

Master of Science

in the College of Arts and Sciences

Georgia State University

2021

ABSTRACT

NADH:quinone oxidoreductase (NQO) from *Pseudomonas aeruginosa* PA01 is an FMN-dependent enzyme that utilizes NADH to catalyze the two-electron reduction of a wide variety of benzoquinones and naphthoquinones. The two-electron quinone reduction by NQO is thought to play a detoxifying role in *P. aeruginosa* PA01 by avoiding the formation of semiquinone radicals known to cause oxidative stress in cells. Crystal structures of NQO demonstrate the enzyme contains two domains: a TIM-barrel domain and an extended domain which are connected through two βα loops. The TIM-barrel domain is the most common enzyme fold found in nature and is often utilized as a target to engineer catalytic functions during the *de novo* synthesis of enzymes. NQO is a mostly unexplored enzyme at the time of this thesis, where only its mechanistic and structural properties have been elucidated. In this thesis, the functional roles of two non-catalytic residues that form the active site of NQO are investigated by employing UV-visible absorption spectroscopy, molecular dynamics, and steady-state kinetics. The thesis presented below highlights the importance of non-catalytic residues in modulating the structural, biophysical, and kinetic properties of NQO, which should be taken into account during the *de novo* synthesis of TIM-barrel containing enzymes.

Previously solved crystal structures of NQO demonstrated the βα loop 3 (residues 75-86) from the TIM-barrel domain samples an open conformation in the ligand-free form and a closed conformation in the ligand-bound form. The relationship between loop 3 rigidity and turnover rates in NQO was investigated by replacing the conserved P78 with a glycine. Circular dichroism, fluorescence spectroscopy, and UV-visible absorption spectroscopy were employed to demonstrate the P78G mutation minimally altered the secondary structure elements of the protein and the active site environment surrounding the flavin cofactor when compared to wild-type NQO.

The gate in NQO was determined to consist of loop 3 and the extended domain, where molecular dynamics demonstrated the substrate-free form of NQO samples more open gate conformations following the P78G mutation. The steady-state kinetic parameters of the mutant and wild-type enzymes revealed the mutation led to a minimal increase in the k_{cat}/K_{CoQ0} value, suggesting the mutation may promote the rate of association with the quinone substrate. The results presented in this investigation suggest the structural rigidity of loop 3 plays a role in modulating domain-domain interactions that may increase the rate of substrate association in NQO.

In the second part of this thesis, the relationship between the protonation state of Y277 and the flavin cofactor's absorption spectrum was investigated in NQO. Y277 is mainly exposed to the solvent in the active site of NQO, with one exception being a 3.0 Å separation between the oxygen atom of Y277 and the C_7 methyl group of the flavin cofactor. The UV-visible absorption spectrum of NQO was investigated as a function of pH and compared to those of a mutant enzyme NQO-Y277F, which indicated Y277 deprotonates at high pH. A combination of UV-visible absorption spectroscopy and QM/MM computations were utilized to determine the effect of Y277 deprotonation on flavin's absorption peak intensities and wavelengths. Both the biochemical experiments and computational calculations suggest that in the absence of solution ions, deprotonating Y277 will significantly alter the absorption spectrum of flavin; however, in the presence of added Na^+ and Cl^- ions, no spectral changes are observed between protonated and unprotonated Y277. QM/MM simulations of NQO with Y277 in the neutral and anionic forms revealed either Na^+ ions move closer to the protein surface and/or Cl^- ions move away from the surface as Y277 deprotonates in the active site. The results presented in this portion of the thesis establish that the solution ions surrounding NQO can interact with the negative point charge at

residue 277 through a long-distance counterion effect to prevent the flavin cofactor's absorption spectrum from being altered.

INDEX WORDS: NADH:quinone oxidoreductase, flavoprotein, gate, UV-visible absorption spectroscopy, fluorescence spectroscopy, circular dichroism, steady-state kinetics, molecular dynamics, principal component analysis, difference contact network analysis, solution ions, quantum mechanics/molecular mechanics, radial distribution function, density functional theory

Functional Importance of Non-Catalytic Residues in the Active Site of NADH:Quinone Oxidoreductase From *Pseudomonas aeruginosa* PA01

by

Benjamin Deen Dratch

Committee Chair: Giovanni Gadda

Committee: Donald Hamelberg

Samer Gozem

Electronic Version Approved:

Office of Graduate Services

College of Arts and Sciences

Georgia State University

May 2021

DEDICATION

This dissertation is dedicated to my grandmother Maxine Hamilton.

ACKNOWLEDGEMENTS

I want to thank my family, friends, and colleagues for assisting me as I complete my masters degree in chemistry. I would like to thank my advisor, Dr. Giovanni Gadda, for teaching me how to thrive in the exciting world of scientific research. Dr. Gadda has played an enormous role in directing my growth from a timid undergraduate student to a confident and proud masters student. I would also like to thank my advisor, Dr. Donald Hamelberg, for allowing me to be a part of his laboratory and explore an entirely new facet of chemistry. My time spent learning computational and biochemical techniques has given me a unique outlook on science that I will forever cherish as I move through my life. For these reasons and many more, I am *incredibly* grateful to both professors. I would also like to give a huge thanks to my laboratory members – Archana, Chris, Renata, Joanna, Daniel, Dan, Maria, Xinqiu, Michael, Dani, Roger, and Jacques. The amount of support I have received from my fellow laboratory members is overwhelming. It has allowed me to build a foundation in scientific research that enables me to achieve my goals and then some. I would also like to give a special thanks to Chris for mentoring me in enzymology and Xinqiu for mentoring me in computational chemistry. I am forever grateful for the time both of you spent helping me better myself. I would also like to give a big thanks to Dr. Samer Gozem and Dr. Yoelvis Orozco-Gonzalez for helping me bring my scientific research to the next level. They have shown me firsthand how to develop a fascinating scientific story by providing their expertise. Finally, I would like to thank my family – Mom, Dad, Sam, and Adrian – and my friends for all of their support. I must be the luckiest person in the world to receive all the love that I do. It is because of this love that I can keep pushing onward no matter what. With the utmost sincerity, thank you to everyone for believing in me.

TABLE OF CONTENTS

LIST OF TABLES

LIST OF FIGURES

LIST OF ABBREVIATIONS

FMN, flavin mononucleotide; TIM, triosephosphate isomerase; IPTG, isopropyl-1-thio-β-D-galactopyranoside; NADH, reduced nicotinamide adenine dinucleotide; NAD^+, oxidized nicotinamide adenine dinucleotide; CoQ_0, Coenzyme-Q_0; NQO, NADH:quinone oxidoreductase; NMO, nitronate monooxygenase; CASPT2, complete active space second-order; ESTM, electrostatic spectral tuning map; MD, molecular dynamics; PCA, principal component analysis; dCNA, difference contact network analysis; QM/MM, quantum mechanics/molecular mechanics

1 INTRODUCTION

1.1 TIM-Barrel Domains in Enzymes

The triosephosphate isomerase (TIM) barrel fold is reported to be among the most versatile enzyme folds and is found in as much as 10% of all enzymes registered in the Protein Data Bank.[1-5] Sequence analysis of the TIM-barrel fold established the fold is associated with 16 different protein families revealing the fold can function as an oxidoreductase, transferase, lyase, hydrolase, or isomerase.[5-8] Structurally, TIM-barrel folds are a type of β-barrel domain comprised of eight parallel β-strands and eight α-helices with βα and αβ loops connecting the secondary structures.[4, 5] The active site residues of TIM-barrel containing enzymes are most often located at the C-terminal ends of the β-stands where the adjacent βα loops form the active site cavity.[5, 9] Previous studies demonstrated βα loops vary in length implying the active site geometry of TIM-barrel containing enzymes is primarily affected by these loops; thus, allowing the enzymes active sites to diversify their functions.[10] In contrast, the portion of TIM-barrel domains located below the active site provides stability to the enzyme by forming a hydrophobic core between the β-strands and α-helices.[7, 9] The distinct functions of the βα loops, that modulate the activity of TIM-barrel containing enzymes, and the hydrophobic core, which provides stability to the enzyme, allows the TIM-barrel domain to be subdivided into two faces known as the 'activity' and 'stability' subunits (**Fig. 1.1**).[7] Previous studies have justified the separation of the TIM-barrel fold into the 'activity' and 'stability' subunits by demonstrating mutations or replacements at βα loops can alter an enzyme's function without a loss is stability.[11, 12] As a result, βα loops are an attractive target for the *de novo* synthesis of TIM-barrel containing enzymes to reengineer catalytic functions.[9]

The synthesis of *de novo* TIM-barrels has previously been utilized to prepare enzymes with altered substrate specificities, reaction rates, thermodynamic stabilities, and catalytic functions.[13-

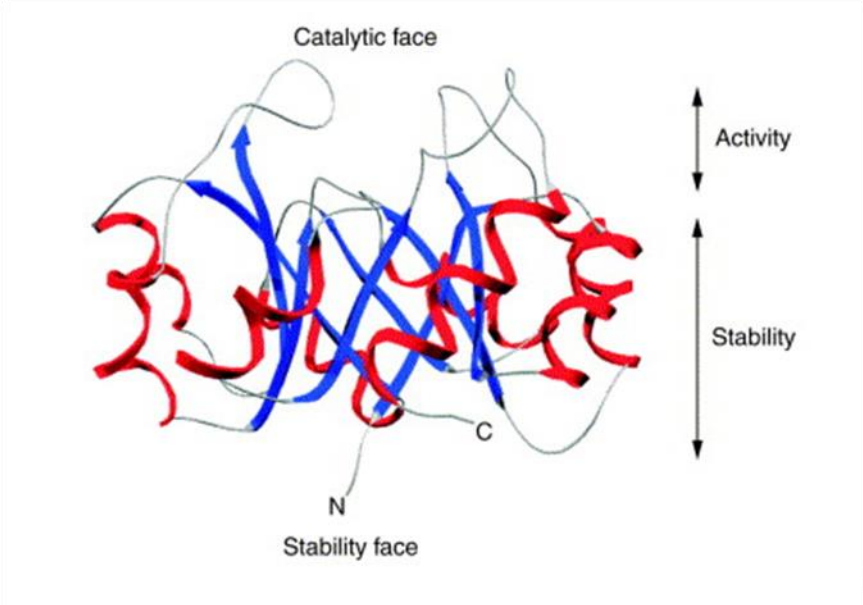

Figure 1.1. Division of Labor in the TIM-Barrel Fold.
Monomeric TrpC from S. solfataricus is illustrated above. β-strands are shown in blue where α-helices are shown in red. The βα loops which connect the C-terminal ends of β-strands to the subsequent α-helices forms the 'catalytic face' of the barrel, which harbors the active site. The remainder of the fold ('stability face') is important for conformational stability. Used with permission from B. Höcker et al., Stability, catalytic versatility, and evolution of the $(\beta\alpha)_8$-barrel fold, Curr. Opin. Biotechnol. 12, 4 (2001) 367-381.

[20] The design of *de novo* TIM-barrel containing enzymes often focuses on replacing catalytic residues located on βα loops to specify the function of the enzyme. However, the low enzymatic efficiencies of *de novo* biocatalysts compared to their counterparts found in nature suggests a better functional understanding of the residues located at the 'activity' subunit of TIM-barrel domains is required to reduce this disparity in catalytic rates.[21-24] To better understand the functions of βα loop residues, the thesis presented below investigates the importance of two non-catalytic residues that form the 'activity' subunit in a TIM-barrel containing enzyme, where the residues are located either directly on a βα loop or on a domain extending from βα loops. A detailed investigation on the relationship between non-catalytic residues in the 'activity' subunit of the TIM-barrel fold and the dynamic, biophysical, and mechanistic properties of TIM-barrel containing enzymes is necessary to reduce the disparity in enzymatic efficiencies between *de novo* and naturally occurring enzymes.

1.2 Previous Studies on NADH:Quinone Oxidoreductase from *Pseudomonas aeruginosa* PA01

NADH:quninone oxidoreductase (NQO, PA1024, EC 1.6.5.9, UniProtKB Q9I4V0) from *Pseudomonas aeruginosa* PA01 is an FMN-dependent enzyme that was recently reclassified from a 2-nitropropane dioxygenase, a class of protein now known as nitronate monooxygenases (NMOs), to its current classification through a kinetic investigation.[25] A quinone reductase is a class of flavin-dependent enzymes that catalyzes two strict hydride transfers: the first from NAD(P)H to the flavin cofactor and the second from the flavin to a quinone.[26] Quinone reductases employ a two-electron transfer onto quinones to ensure the formation of the hydroquinone species, thereby avoiding semiquinone radical species generated by one-electron transfers (**Fig. 1.2**).[27] Semiquinone radicals react with molecular oxygen to form reactive oxygen species, which leads to oxidative stress in cells resulting in tissue degeneration, apoptosis, premature aging, and neoplasia.[28, 29] It is thought that NQO plays an essential role in the cellular detoxification of *P. aeruginosa* PA01 by avoiding the generation of harmful quinone species that lead to cytotoxicity. In contrast, the physiological significance of quinone reductases utilizing NAD(P)H as the reducing substrate is not as well understood compared to the significance of the quinone reduction. The importance of NQO utilizing NADH as the reducing substrate was investigated by analyzing the genomic context of NQO. The study demonstrated that the operon encoding for NQO also contains hypothetical acyl-CoA dehydrogenases, a short-chain dehydrogenase, an acyl-CoA hydratase/isomerase, and a porin, suggesting NQO may be translated with these enzymes to play a role in the β-oxidation pathway of *P. aeruginosa* PA01.[25] Previous studies hypothesized NQO plays a role in the β-oxidation pathway by oxidizing NADH to maintain a ratio of $[NAD^+]/[NADH]$ favorable for the catabolism of fatty acid chains.[30, 31]

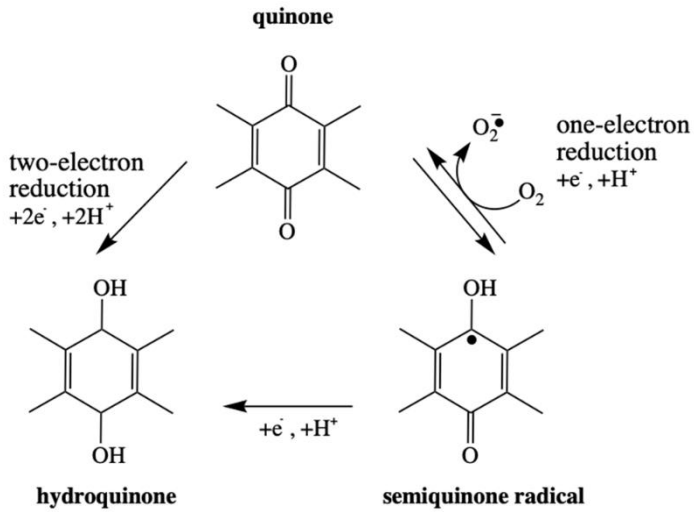

Figure 1.2. Reduction Mechanism of Quinones.
Formation of the hydroquinone is achieved by a two-electron reduction onto the oxidized quinone, whereas a one-electron reduction of quinones forms the semiquinone radical species. Semiquinone radical species can reduce molecular oxygen to form reaction oxygen species. Used with permission from S. Deller et al., Flavin-dependent quinone reductases, Cell. Mol. Life Sci. 65 (2008) 141-160.

NQO's original classification as an NMO resulted from a qualitative inhibition assay, a gene function prediction, and a crystal structure of NQO with 2-nitropropane bound in the active site, suggesting the enzyme functioned as an NMO.[32] The classification as an NMO was uncontested until 8 years later when the structural motifs characteristic of class I NMOs were established.[33] A comparison between the structural motifs of NQO and class I NMOs demonstrated NQO does not contain any of the conserved structural sequences characteristic of class I NMOs. This discovery prompted a reevaluation of NQO's function through a mechanistic investigation, which revealed the enzyme does not exhibit activity as an NMO; rather, NQO efficiently reacts with NADH and a wide variety of quinones as an oxidoreductase.[25] The structural motifs for NQO were also reevaluated and compared to proteins annotated in the sequence database GenBankTM, which revealed ~500 hypothetical proteins with the same conserved structural sequences. All ~500 hypothetical proteins containing the same structural motifs as NQO were annotated as NMOs, much like NQO prior to a kinetic investigation.[25] The bioinformatic and kinetic study on NQO

determined the hypothetical proteins sharing the same structural motifs as NQO needed to be reclassified, which lead to the formation of a new class of NADH:quinone oxidoreductases.[25]

The crystal structure of NQO was solved in the ligand-free form (PDB: 2GJL) and in complex with NAD^+ (PDB: 6E2A), which is the product of NADH oxidation from the reductive half-reaction catalyzed by the enzyme.[32, 34] Both ligand-bound and ligand-free crystal structures identified two domains in NQO: a TIM-barrel domain (M^1 – P^{211} and E^{299} – V^{328}) and an extended domain (Ile^{212} – Asp^{298}) connected by βα loops 7 and 8 (**Fig. 1.3**). One molecule of FMN was found to be noncovalently bound in the active site pocket of both crystal structures of NQO. Structural analysis of FMN bound in NQO suggests the cofactor forms hydrogen bonds between its phosphate moiety and the protein backbone amide atoms of Ala150, Gly180, Gly201, and

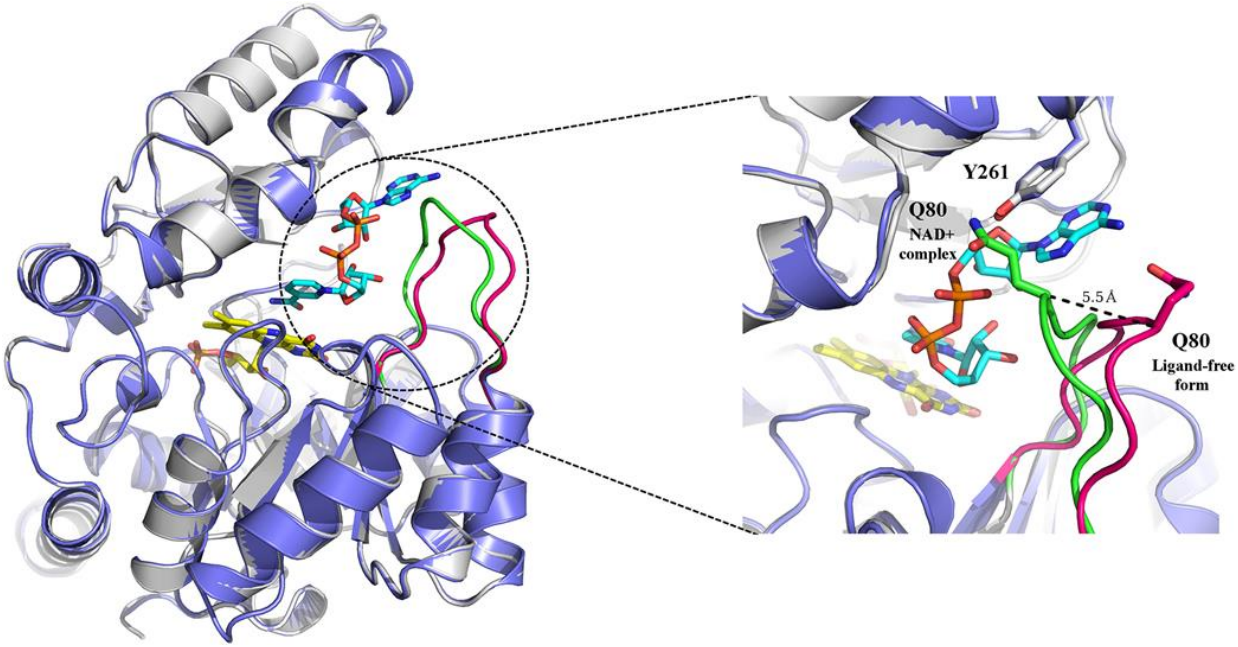

Figure 1.3. Superimposed Structures of Ligand-Free and Ligand-Bound NQO.
The overall structure of the ligand-free form of NQO (PDB: 2GJL) is in blue and the NQO-NAD^+ complex (PDB: 6E2A) is in grey. The βα loop 3 (residue 75-86) is highlighted in pink (ligand-free form) and green (NQO-NAD^+ complex). The FMN carbons are in yellow and the NAD^+ carbons are in cyan. The dashed line represents the distance between the position of the Cα atom of Q80 in the ligand-free and ligand-bound structures. Used with permission from J. Ball et al., Steric hindrance controls pyridine nucleotide specificity of flavin-dependent NADH:quinone oxidoreductase, Protein Sci. 28, 1 (2019) 167-175.

Thr202 to remain bound within the protein.[32] The interactions that form between NQO and NAD^+ were also investigated, which established the enzyme binds the product to its active site pocket through several hydrogen bonds stemming from the FMN cofactor, the extended domain, and the βα loop 3 (residues 75-86) from the TIM-barrel domain.[34] A comparison between the crystal structures of NQO with and without NAD^+ revealed loop 3 adopts two conformations near the site of NAD^+ binding, suggesting the loop acts as a gate to modulate the formation of the enzyme-substrate complex (**Fig. 1.3**).[34] The conformational change in loop 3 is thought to facilitate a hydrogen bond interaction between the residues Q80 in loop 3 and Y261 in the extended domain to secure the substrate in the active site of NQO (**Fig. 1.3**). Loop 3 contains three proline residues (P78, P82, and P84), hypothesized to provide an internal rigidity to the backbone of the loop, which is required for the proper conformational changes to take place within the gate of NQO.[34] At present, the mechanistic and structural analysis of NQO are the only studies found in the literature that investigate the recently defined class of NADH:quinone oxidoreductases.

1.3 Specific Goal

The specific goal of this thesis is to investigate the functional significance of non-catalytic residues that form the 'activity' subunit of the TIM-barrel domain in NQO using UV-visible absorption spectroscopy, molecular dynamics, and steady-state kinetics. The three proline residues located on the βα loop 3 are hypothesized to provide structural rigidity to the loop, which allows the gate in NQO to adopt the conformational changes necessary to facilitate substrate binding. The structural residue P78 is the only proline on loop 3 that is conserved within the second structural motif characteristic of a new class of NADH:quinone oxidoreductases (^{66}TXXPFGVNXThhP^{78}, where h is any hydrophobic residue and X is any residue). Thus, we hypothesize the structural

rigidity provided by P78 to loop 3 is required to maintain proper gate conformations that modulate the rate of substrate association in NQO.[25]

Y277 is an active site residue located on the extended domain of NQO that is positioned 3.0 Å from the C_7 methyl group of the FMN cofactor. Apart from the flavin, Y277 is surrounded by the bulk solvent in the active site. The C_7 methyl group of flavin is located on the non-catalytic portion of the flavin cofactor; thus, we hypothesize Y277 does not directly contribute electrons to the oxidation-reduction reactions performed by NQO. Instead, the proximity of Y277 to the flavin suggests NQO can be utilized as a model system to elucidate further the relationship between flavin's electrostatic environment and its absorption spectrum. A comprehensive spectral, computational, and kinetic characterization of the two active site residues located either on a βα loop or a domain extending from βα loops in NQO is pursued below. This study will provide the first structure-function-dynamic investigation of key residues in the recently reclassified enzyme NQO from *P. aeruginosa* PA01. This study's broader impact serves to help reduce the disparity in enzymatic efficiencies between *de novo* and naturally occurring enzymes by demonstrating the functional significance of non-catalytic residues in the 'activity' subunit of TIM-barrel containing enzymes, which may be overlooked in current protein engineering studies.

1.4 References

[1] Copley, R. R., and Bork, P. (2000) Homology among (βα)8 barrels: implications for the evolution of metabolic pathways11Edited by G. Von Heijne, *J. Mol. Biol. 303*, 627-641.

[2] Gerlt, J. A. (2000) New wine from old barrels, *Nat. Struct. Biol. 7*, 171-173.

[3] Gerlt, J. A., and Babbitt, P. C. (2001) Barrels in pieces?, *Nat. Struct. Biol. 8*, 5-7.

[4] Richard, J. P., Zhai, X., and Malabanan, M. M. (2014) Reflections on the catalytic power of a TIM-barrel, *Bioorg. Chem. 57*, 206-212.

[5] Wierenga, R. K. (2001) The TIM-barrel fold: a versatile framework for efficient enzymes, *FEBS Lett. 492*, 193-198.

[6] Hegyi, H., and Gerstein, M. (1999) The relationship between protein structure and function: a comprehensive survey with application to the yeast genome 11Edited by G. von Heijne, *J. Mol. Biol. 288*, 147-164.

[7] Höcker, B., Jürgens, C., Wilmanns, M., and Sterner, R. (2001) Stability, catalytic versatility and evolution of the (βα)8-barrel fold, *Curr. Opin. Biotechnol. 12*, 376-381.

[8] Nagano, N., Gail Hutchinson, E., and Thornton, J. M. (1999) Barrel structures in proteins: Automatic identification and classification including a sequence analysis of TIM barrels, *Protein Sci. 8*, 2072-2084.

[9] Caldwell, S. J., Haydon, I. C., Piperidou, N., Huang, P.-S., Bick, M. J., Sjöström, H. S., Hilvert, D., Baker, D., and Zeymer, C. (2020) Tight and specific lanthanide binding in a de novo TIM barrel with a large internal cavity designed by symmetric domain fusion, *Proc. Natl. Acad. Sci. U.S.A. 117*, 30362.

[10] Richard, J. P., Amyes, T. L., Goryanova, B., and Zhai, X. (2014) Enzyme architecture: on the importance of being in a protein cage, *Curr. Opin. Chem. Biol. 21*, 1-10.

[11] Petsko, G. A. (2000) Design by necessity, *Nature 403*, 606-607.

[12] Thanki, N., Zeelen, J. P., Mathieu, M., Jaenicke, R., Abagyan, R. A., Wierenga, R. K., and Schliebs, W. (1997) Protein engineering with monomeric triosephosphate isomerase (monoTIM): the modelling and structure verification of a seven-residue loop, *Protein Eng. Des. Sel. 10*, 159-167.

[13] Blomberg, R., Kries, H., Pinkas, D. M., Mittl, P. R. E., Grütter, M. G., Privett, H. K., Mayo, S. L., and Hilvert, D. (2013) Precision is essential for efficient catalysis in an evolved Kemp eliminase, *Nature 503*, 418-421.

[14] Giger, L., Caner, S., Obexer, R., Kast, P., Baker, D., Ban, N., and Hilvert, D. (2013) Evolution of a designed retro-aldolase leads to complete active site remodeling, *Nat. Chem. Biol. 9*, 494-498.

[15] Khersonsky, O., Röthlisberger, D., Wollacott, A. M., Murphy, P., Dym, O., Albeck, S., Kiss, G., Houk, K. N., Baker, D., and Tawfik, D. S. (2011) Optimization of the In-Silico-Designed Kemp Eliminase KE70 by Computational Design and Directed Evolution, *J. Mol. Biol. 407*, 391-412.

[16] Obexer, R., Godina, A., Garrabou, X., Mittl, P. R., Baker, D., Griffiths, A. D., and Hilvert, D. (2017) Emergence of a catalytic tetrad during evolution of a highly active artificial aldolase, *Nature Chem. 9*, 50.

[17] Preiswerk, N., Beck, T., Schulz, J. D., Milovník, P., Mayer, C., Siegel, J. B., Baker, D., and Hilvert, D. (2014) Impact of scaffold rigidity on the design and evolution of an artificial Diels-Alderase, *Proc. Natl. Acad. Sci. U.S.A.111*, 8013.

[18] Privett, H. K., Kiss, G., Lee, T. M., Blomberg, R., Chica, R. A., Thomas, L. M., Hilvert, D., Houk, K. N., and Mayo, S. L. (2012) Iterative approach to computational enzyme design, *Proc. Natl. Acad. Sci. U.S.A. 109*, 3790.

[19] Sharma, P., Kaila, P., and Guptasarma, P. (2016) Creation of active TIM barrel enzymes through genetic fusion of half-barrel domain constructs derived from two distantly related glycosyl hydrolases, *FEBS J. 283*, 4340-4356.

[20] Wang, J., Zhang, T., Liu, R., Song, M., Wang, J., Hong, J., Chen, Q., and Liu, H. (2017) Recurring sequence-structure motifs in (βα)8-barrel proteins and experimental optimization of a chimeric protein designed based on such motifs, *Biochim. Biophys. Acta Proteins Proteomics 1865*, 165-175.

[21] Basanta, B., Bick, M. J., Bera, A. K., Norn, C., Chow, C. M., Carter, L. P., Goreshnik, I., Dimaio, F., and Baker, D. (2020) An enumerative algorithm for de novo design of proteins with diverse pocket structures, *Proc. Natl. Acad. Sci. U.S.A. 117*, 22135.

[22] France, S. P., Hepworth, L. J., Turner, N. J., and Flitsch, S. L. (2017) Constructing Biocatalytic Cascades: In Vitro and in Vivo Approaches to de Novo Multi-Enzyme Pathways, *ACS Catal. 7*, 710-724.

[23] Gora, A., Brezovsky, J., and Damborsky, J. (2013) Gates of Enzymes, *Chem. Rev. 113*, 5871-5923.

[24] Röthlisberger, D., Khersonsky, O., Wollacott, A. M., Jiang, L., DeChancie, J., Betker, J., Gallaher, J. L., Althoff, E. A., Zanghellini, A., Dym, O., Albeck, S., Houk, K. N., Tawfik, D. S., and Baker, D. (2008) Kemp elimination catalysts by computational enzyme design, *Nature 453*, 190-195.

[25] Ball, J., Salvi, F., and Gadda, G. (2016) Functional Annotation of a Presumed Nitronate Monoxygenase Reveals a New Class of NADH:Quinone Reductases, *J. Biol. Chem. 291*, 21160-21170.

[26] Deller, S., Macheroux, P., and Sollner, S. (2007) Flavin-dependent quinone reductases, *Cell. Mol. Life Sci. 65*, 141.

[27] Iyanagi, T., and Yamazaki, I. (1970) One-electron-transfer reactions in biochemical systems V. Difference in the mechanism of quinone reduction by the NADH dehydrogenase and the NAD(P)H dehydrogenase (DT-diaphorase), *Biochim. Biophys. Acta Bioenerg. 216*, 282-294.

[28] Brunmark, A., and Cadenas, E. (1989) Redox and addition chemistry of quinoid compounds and its biological implications, *Free Rad. Biol. Med. 7*, 435-477.

[29] Ezraty, B., Gennaris, A., Barras, F., and Collet, J.-F. (2017) Oxidative stress, protein damage and repair in bacteria, *Nature Rev. Microbiol. 15*, 385.

[30] Green, D. E., Mii, S., Mahler, H. R., and Bock, R. M. (1954) Studies on the fatty acid oxidizing system of animal tissues: III. Butyryl coenzyme A dehydrogenase, *J. Biol. Chem. 206*, 1-12.

[31] Lê-Quôc, D., and Lê-Quôc, K. (1989) Relationships between the NAD(P) redox state, fatty acid oxidation, and inner membrane permeability in rat liver mitochondria, *Arch. Biochem. Biophys. 273*, 466-478.

[32] Ha, J. Y., Min, J. Y., Lee, S. K., Kim, H. S., Kim, D. J., Kim, K. H., Lee, H. H., Kim, H. K., Yoon, H.-J., and Suh, S. W. (2006) Crystal Structure of 2-Nitropropane Dioxygenase Complexed with FMN and Substrate: Identification of the Catalytic Base, *J. Biol. Chem. 281*, 18660-18667.

[33] Salvi, F., Agniswamy, J., Yuan, H., Vercammen, K., Pelicaen, R., Cornelis, P., Spain, J. C., Weber, I. T., and Gadda, G. (2014) The Combined Structural and Kinetic Characterization of a Bacterial Nitronate Monooxygenase from *Pseudomonas aeruginosa* PAO1 Establishes NMO Class I and II, *J. Biol.Chem. 289*, 23764-23775.

[34] Ball, J., Reis, R. A. G., Agniswamy, J., Weber, I. T., and Gadda, G. (2019) Steric hindrance controls pyridine nucleotide specificity of a flavin-dependent NADH:quinone oxidoreductase, *Protein Sci. 28*, 167-175.

2 INCREASED MOBILITY OF LOOP 3 WIDENS GATE DYNAMICS WHILE PRESERVING ENZYME FUNCTION IN NADH:QUINONE OXIDOREDUCTASE

2.1 Abstract

Enzymes are essential for all living organisms and often require a series of dynamic motions to maintain efficient turnover rates. Dynamics ranging from large and prominent domain motions to small and subtle amino acid fluctuations play a key role in catalysis. However, the link between protein dynamics and catalysis is currently insufficiently well understood, as demonstrated by the low enzymatic efficiencies of *de novo* enzymes. The crystal structures of NADH:quinone oxidoreductase from *Pseudomonas aeruginosa* PA01 (NQO) reveal that loop 3 (residues 75-86) of the TIM-barrel domain is displaced by 5.5 Å towards the active site following NAD^+ binding to NQO. Thus, loop 3 is proposed to act as a gate that stabilizes the enzyme-substrate complex by forming hydrogen bond interactions with the substrate and the extended domain of NQO. Loop 3 contains three proline residues thought to provide structural rigidity to the loop, where only P78 is conserved in the second structural motif of NQOs. In this study, P78 was mutated to glycine to decrease the protein backbone's internal rigidity at loop 3. The circular dichroism, fluorescence, and UV-visible absorption spectra were determined with NQO-P78G and NQO-WT, which revealed the P78G mutation minimally affects the protein's secondary structure elements and flavin's active site microenvironment in NQO. Molecular dynamics with NQO-P78G and NQO-WT with and without NAD^+ bound demonstrated that NQO-P78G in the ligand-free form samples wider conformations at the extended domain and loop 3, which opens up the gate to expose the active site of NQO to the bulk solvent. Steady-state kinetic parameters were determined for the mutant and wild-type enzymes at varying concentrations of NADH and Coenzyme-Q_0 at pH 6.0. The results established a 3.5-fold increase in the K_{CoQ0} value, a 2.0-fold decrease in the k_{cat}

value, and a 1.8-fold increase in the k_{cat}/K_{CoQ0} value in NQO-P78G compared to NQO-WT. Overall, the results presented below suggest that decreasing the rigidity at loop 3 alters the gate's preferred conformation states to sample more open conformations without significantly affecting the active site microenvironment or kinetic mechanism of NQO.

2.2 Introduction

Enzymes are essential for all living organisms and often require a series of dynamic motions to maintain efficient catalytic rates.[1-3] Dynamics ranging from large and prominent domain motions[4-9] to small and subtle amino acid fluctuations[10-14] are known to play a key role in catalysis. The fluctuations of the protein backbone alone do not determine enzyme function; instead, the enzyme's functional outcome is determined by the multiple conformational states these motions encode.[1, 3, 15-21] Flexible regions of enzymes can alternate between active and inactive conformational states, which makes these protein regions a promising target for the design of allosteric drugs.[22-26] In comparison, dynamic motions associated with enzyme turnover have been suggested to be insufficiently well understood as demonstrated by low enzymatic efficiencies of *de novo* biocatalysts.[2, 27-34] To design better *de novo* biocatalysts and allosteric drugs that target flexible regions encoding inactive conformations, there is a need for a better understanding of the functional dynamics and catalytic roles of flexible protein regions.

Proteins often contain dynamic regions known as gates which consist of residues, loops, secondary structures, or domains that adopt open and closed conformations.[2, 35] Gate dynamics sample active and inactive conformations that control the specificity and access of substrates, products, ions, or solvents to the interior of a protein.[35-39] From a mechanistic point of view, gates can be involved in two processes. Firstly, gates can modulate substrate binding or product release by forming a path between the active site pocket and the bulk solvent.[13, 40] Secondly, gates can

modulate reaction rates by preparing an active site environment required for reaction intermediates to form.[41, 42] Gating residues and loops are attractive targets for protein engineering studies since they tend to be the natural site for mutations that persist during protein evolution.[43-45] Site-directed mutagenesis studies on gating residues have shown that gates are an effective target to alter the substrate specificity[45-47], enantioselectivity[48-50], or thermostability[51-53] of enzymes. An analysis of the molecular functions and structural characteristics of 129 molecular gates led to the formation of a gate classification system, where gates are grouped into six structural classes with three major functions and locations.[2] The analysis of protein gates provides a classification scheme that can be easily expanded to encourage the study and engineering of gates; however, the system has not been updated since its conception in 2013. Hence, there is a need to further study and characterize enzyme gates to ensure the current classification system of gates applies to all proteins.

NADH:quinone oxidoreductase (NQO, EC 1.6.5.9, UniProtKB Q9I4V0) from *P. aeruginosa* PA01 is an FMN-dependent enzyme that utilizes NADH as the reducing substrate to catalyze the two-electron reduction of a wide variety of quinones.[54] The physiological role of NQO is unknown; however, the enzyme's preferred substrates and genomic context suggest that NQO serves a dual function in the cell by detoxifying quinones and maintaining a ratio of $[NAD^+]/[NADH]$ that is favorable for the β-oxidation pathway.[55-57] Previously solved crystal structures of NQO demonstrated the enzyme consists of a TIM-barrel domain and an extended domain, where the two domains are connected by a hinge region to form the active site pocket.[58] According to the Protein Data Bank, the TIM-barrel fold is the most common enzyme fold and is found in 10% of all enzymes.[59-61] TIM-barrel domains are composed of eight parallel β-strands, at the center of the fold, and eight α-helices with βα and αβ loops connecting the secondary structures. βα loops are located at the C-terminal ends of the β-strands and are especially crucial for the

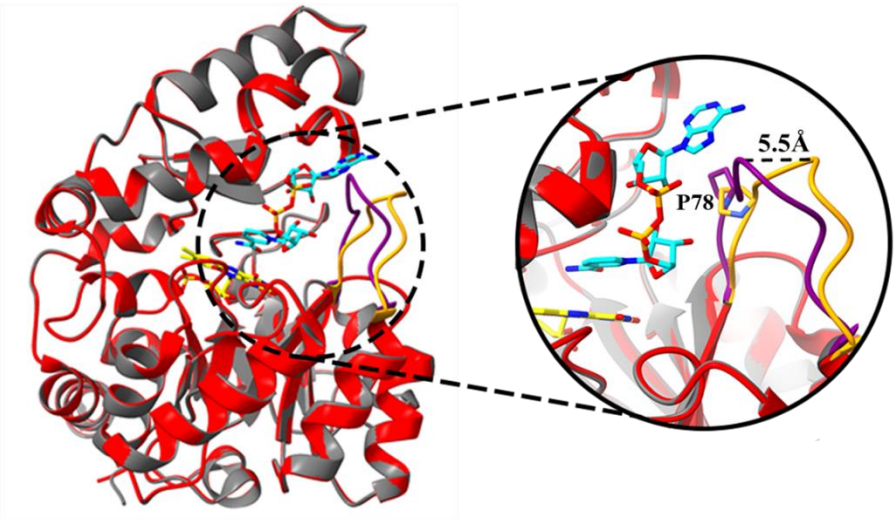

Figure 2.1. Superimposed Structures of NQO With and Without NAD$^+$ Bound in the Active Site.
The overall structure of the ligand-free form of NQO is in red (PDD: 2GJL) and the ligand-bound complex is in grey (PDB: 6E2A). Loop 3 is highlighted in yellow for the ligand-free form and purple for the ligand-bound form. Yellow sticks depict the FMN carbons while the NAD$^+$ carbons are colored in cyan. The area around loop 3 is magnified to demonstrate the conformational change at loop 3 following substrate binding. The dashed line depicts the distance traveled by the Cα atom of Q80, which hydrogen bonds to Y271 of the extended domain in the ligand-bound form.

activity of TIM-barrel containing enzymes since the loops' variable lengths primarily form the active site geometry.[61, 62] Previous studies have established that mutations on βα loops can alter an enzyme's function without perturbing the stability the TIM-barrel fold; thus, βα loops are an ideal target to study the structure-function-dynamic relationships in enzymes.[63-67]

The crystal structures for NQO with and without NAD$^+$ bound in the active site have recently been solved.[58, 68] A comparison of the ligand-bound and ligand-free crystal structures of NQO revealed a mobile βα loop (loop 3, residues 75-86) that is displaced by 5.5 Å towards the active site following ligand binding (**Fig. 2.1**). A previous study hypothesized that loop 3 acts as a gate to secure NADH to the active site pocket of NQO by changing conformations to form a hydrogen bond between the residues Q80 on loop 3 and Y261 near the interrupted helix (residues 268-270) of the extended domain.[58] Interestingly, a short region of loop 3 (residues 75-78) is

conserved in the second structural motif characteristic of a new class of NADH:quinone oxidoreductases (^{66}TXXPFGVNXThhP^{78}, where h is any hydrophobic residue and X is any residue).[54, 68] Loop 3 contains three proline residues thought to provide structural rigidity to the loop and allow for the proper gate conformations to be sampled. Of the residues included in the second structural motif of NQO, only one of the three prolines on loop 3 (P78) is conserved, suggesting that the conserved proline may play an important role in the loop's gating function. In this study, the significance of loop 3 conformations in modulating substrate binding was investigated by mutating the conserved P78 to a glycine (NQO-P78G) to reduce the backbone rigidity at loop 3. The Cα of P78 is 11.8 Å from the N_3 atom of the FMN cofactor; thus, we hypothesize that mutating the conserved P78 will not perturb the active site environment of NQO. Instead, the P78G mutant is expected to destabilize the dynamics of loop 3 and increase the rate of enzyme-substrate association by sampling more open conformations at the gate in NQO. A combination of molecular dynamics and steady-state kinetics were used to determine how reducing the rigidity of the protein backbone at loop 3 alters the function of NQO.

2.3 Experimental Procedures

2.3.1 Materials

The enzymes *Pfu* DNA polymerase and *Dpn*I were purchased from Stratagene (La Jolla, CA) and New England Biolabs (Ipswich, MA), respectively. QIAprep Spin Miniprep Kit and QIAquick PCR purification kit were from Qiagen (Valencia, CA). CutSmart Buffer and Deoxynucleotide Solution Mix were obtained from New England Biolabs (Ipswich, MA). Oligonucleotides containing the P78G point mutation were purchased from Sigma Genosys (The Woodlands, TX). Isopropyl-1-thiol-β-D- galactopyranoside (IPTG) was ordered from Promega (Madison, WI). *Escherichia coli* strains DH5α and Rosetta(DE3)pLysS were purchased from

Invitrogen Life Technologies (Grand Island, NY) and Novagen (Madison, WI), respectively. HiTrapTM Chelating HP 5 mL affinity column and prepacked PD-10 desalting columns were obtained from GE Healthcare (Piscataway, NJ). All other reagents used were of the highest purity commercially available.

2.3.2 Site-Directed Mutagenesis and Purification of NQO-P78G

NQO-P78G was prepared using mutagenic polymerase chain reaction (PCR) with *E. coli* strain DH5α harboring the pET20b(+)/*pa*1024 plasmid as a template.[54] PCR products were purified using the QIAquick PCR Purification Kit, digested with *Dpn*I, and transformed to chemically competent DH5α cells via the heat shock method.[69] The mutant plasmids were extracted and purified using the QIAquick Spin Miniprep Kit and sequenced at Macrogen Inc (Rockville, MD). NQO-P78G was expressed in *E. coli* strain Rosetta(DE3)pLysS and purified using methods previously described for the wild-type enzyme.[54] The purified NQO-P78G was stored at −20 °C in 20 mM sodium phosphate, pH 8.0, 100 mM sodium chloride, and 10% glycerol.

2.3.3 Circular Dichroism

Circular dichroism spectra were acquired for NQO-P78G and NQO-WT using a Jasco (Easton, MD) J-1500 Circular Dichroism Spectrophotometer. Samples were passed through a PD-10 desalting column to separate contaminants and denatured proteins before use. Enzyme samples were diluted to a concentration of 0.1 mg/mL flavin-bound enzyme in 20 mM potassium phosphate, pH 7.0, and 200 mM sodium chloride. Spectra were recorded at 25 °C using a 1 mm path length quartz cuvette with a bandwidth of 2 nm and a scanning speed of 20 nm/min. The resulting CD spectra were corrected for buffer contributions, smoothed by the Means-Movement method, and subsequently analyzed using the Jasco Spectra Analysis program.

2.3.4 Fluorescence Spectroscopy

Fluorescence excitation and emission spectra for NQO-P78G, NQO-WT, and free-FMN were measured using a Shimadzu (Kyoto, Japan) model RF-5301 PC spectrofluorometer with a 1 cm path length quartz cuvette at 15 °C. Enzyme-bound FMN and free-FMN were measured at a final concentration of 3 μM and 1 μM, respectively. Fluorescence parameters were determined in 20 mM potassium phosphate, pH 6.0, and 200 mM sodium chloride, where the enzyme buffer was exchanged using a PD-10 desalting column before use. Fluorescence spectra were corrected for Rayleigh and Raman scattering, and spectral figures were prepared using KaleidaGraph software (Synergy Software, Reading, PA).

2.3.5 UV-Visible Absorption Spectroscopy

UV-visible absorption spectra were recorded using an Agilent Technologies model HP 8453 PC diode-array spectrophotometer (Santa Clara, CA) equipped with a thermostated water bath. Heat denaturation was used to extract the enzyme-bound FMN from NQO-P78G to determine the mutant's extinction coefficient values.[70] Enzymes were denatured at 100 °C for 20 and 30 minutes then removed from the solution via centrifugation at 14,000 rpm. The concentration of released FMN was calculated using the molar extinction coefficient for free FMN, $\varepsilon_{450\ nm}$ = 12,200 $M^{-1}cm^{-1}$, at 25 °C.[71] The concentration of the flavin-bound NQO-P78G was calculated using the experimentally determined extinction coefficient $\varepsilon_{461\ nm}$ = 11,900 $M^{-1}cm^{-1}$ (this study). The total protein concentration was determined using the Bradford method with bovine serum albumin as a standard.[72]

The UV-visible absorption spectra for NQO-P78G and NQO-WT were measured as a function of pH in 10 mM sodium phosphate, 10 mM sodium pyrophosphate, pH 8.0, and 100 mM sodium chloride at 15 °C. Absorption spectra were recorded while gradually increasing pH by

adding 10 µL volumes of 1 M sodium hydroxide to a final pH of 11.5 while stirring. After each sodium hydroxide addition, the enzyme solution was allowed to equilibrate until no changes in the pH value and absorption spectra were observed, which typically required 2-3 min. Resulting spectra were corrected for protein concentration below 325 nm using $\varepsilon_{461\ nm}$ = 11,900 $M^{-1}cm^{-1}$ for NQO-P78G and ε_{461} = 12,400 $M^{-1}cm^{-1}$ for NQO-WT[54].

2.3.6 Molecular Dynamics

Multiple microsecond-long Molecular dynamic (MD) simulations were performed on four systems, each containing an FMN cofactor: (i) NQO-P78G, (ii) NQO-WT, (iii) NQO-P78G with bound NAD^+, and (iv) NQO-WT with bound NAD^+. Initial coordinates for MD simulations were from the crystal structures of NQO-WT in the substrate-free form (PDB: 2GJL) or with NAD^+ (PDB: 6E2A). MD simulations were performed using AMBER 16 along with the AMBER ff14SB force-field.[73, 74] Force-field parameters for the FMN cofactor were taken from S*ü*hnel *et al.*[75] NQO-P78G was prepared *in silico* by altering the amino acid sequence in the NQO-WT PDB files and removing the side chain atoms at the residue of interest. The AmberTools xleap program was used to construct the appropriate system required for each MD simulation by adding back the missing sidechain atoms. Each system was solvated in a 10 Å TIP3P octahedral box, containing two Cl^- ions to neutralize the system.[76, 77] The energy minimization involved 2,000 steps of steepest descent followed by 3,000 steps of conjugate gradient, where harmonic restraints held the position of the solute. Five rounds of energy minimization were performed, where the force constant of the positional restraint was gradually reduced from 500 to 0 kcal mol^{-1} $Å^{-2}$. Each system was then heated from 100 to 300 K within 500 ps under NVT periodic conditions with a 1-fs time step. Five rounds of heating were performed, where the force constant of restraint was set to 500, 300, 100, 50, and 5 kcal mol^{-1} $Å^{-2}$. A 1-ns equilibration step was performed with a 2-fs time step where the

whole system was allowed to move freely. All simulations were run under NPT (300 K, 1 bar) periodic conditions where the temperature was regulated used the Langevin thermostat through a 1 ps^{-1} collision frequency. Simultaneously, the pressure was controlled using the Monte Carlo barostat with a coupling constraint of 1 ps. Long-range non-bonded electrostatic interactions were evaluated using the particle mesh Ewald (PME) method with a cutoff of 9 Å.[78] All bonds involving hydrogen atoms were constrained using the SHAKE algorithm.[79] Productions for NQO-WT and NQO-WT with NAD^+ were run for 1 μs while NQO-P78G and NQO-P78G with NAD^+ were simulated for 3.5 μs and 1.5 μs, respectively. The subsequent analysis utilized the last 800 ns of the NQO-WT, NQO-WT with NAD^+, and NQO-P78G with NAD^+ trajectories, and the last 1.6 μs of the NQO-P78G trajectory.

2.3.7 Principal Component Analysis and Distance Calculations

Principal component analysis (PCA) was applied to all four systems using the CPPTRAJ module of AMBER16.[80] Structures were superimposed to the backbone atoms (N, Cα, C, and O) of the first frame of the NQO-WT simulation. The variance-covariance matrix characterizing correlated internal backbone motions was calculated and diagonalized to obtain eigenvectors and eigenvalues. Eigenvectors were projected back onto all four systems' trajectories to obtain the principal components (PCs), which describes the structural variance between the simulations captured at each PC. The top two PCs (PC1 and PC2) captured the most significant structural variance and were projected onto a 2-D PC plot using ggplot2 to analyze the interconformer relationship between trajectories.[81] The motions captured by PC1 and PC2 were visualized using VMD.[82] To measure fluctuations of the gate in NQO, the distance between the Cα atoms of Q80 and Y261 was calculated and analyzed using CPPTRAJ, Bio3D, and R packages.[83, 84] The

fluctuations of the gate in NQO were monitored by first superimposing structures on the basis of the backbone atoms then calculating the separation between the gate residues.

2.3.8 Difference Contact Network Analysis

Residue-residue contacts were analyzed for NQO-P78G and NQO-WT following methods previously described.[85, 86] A contact was defined to have formed between residues if the heavy atoms of two residues, at least three amino acids apart in the protein sequence (i to i + n, $n \geq 3$), were within 4.5 Å from each other. Previous studies have determined a 4.5 Å cutoff to be optimal for contact analysis as it considers the range of interactions between amino acid residues.[86, 87] The probability that residue contacts would form was evaluated, and the contact probability difference of NQO-WT to NQO-P78G was generated to assess how contacts were affected by the mutation. The contact probability changes were further elucidated by using the difference contact network analysis (dCNA) method.[88, 89] The use of dCNA allows changes in residue-residue contacts between protein regions to be easily identified better to understand the conformational changes between any two systems. The analysis and subsequent figures were prepared using Bio3D[83, 84], and in-house R scripts.

2.3.9 Enzymatic Assays

The steady-state kinetic parameters were measured with an Agilent Technologies (Santa Clara, CA) model HP 8453 PC diode-array spectrophotometer equipped with a thermostated water bath. The initial rates of the reaction were monitored in 20 mM potassium phosphate, pH 6.0, and 100 mM sodium chloride at 25 °C.[90] Turnover of NQO was monitored by varying concentrations of NADH from 10 – 200 µM and CoenzymeQ_0 (CoQ_0) from 2 – 150 µM with a final enzyme concentration of 100 nM in the reaction mixture. Stock solutions of CoQ_0 were prepared in 100% ethanol so that the final concentration of ethanol in the reaction mixture was kept at 1% to prevent

any effect of ethanol on enzyme activity. Reaction rates were measured by following NADH consumption at 340 nm, using ε_{340} = 6,220 M^{-1} cm^{-1}.[91, 92] The enzymatic reactions were initiated by the addition of NQO at a final concentration of 100 nM.

2.3.10 Data analysis

Kinetic data were fit using Kinetic Studio Software Suite Enzfitter (Hi-Tech Scientific, Bradford on Avon, U.K.). Steady-state kinetic parameters at varying concentrations of NADH (A) and CoQ_0 (B) were determined by fitting the initial rates of reactions to the Michaelis-Menten equations. Equation 1 describes a ping-pong bi-bi steady-state mechanism, while equation 2 describes the same mechanism but accounts for substrate inhibition by NADH. Initial rates were measured by taking the ratio of the reaction's initial velocity (v_0) and the enzyme concentration (e). K_a represents the Michaelis-Menten constant for NADH, K_b represents the Michaelis-Menten constant for CoQ_0, k_{cat} is the turnover number of the enzyme at saturating concentrations of both substrates, and K_{ia} is the inhibition constant that describes the binding of NADH to the reduced form of enzyme yielding a dead-end complex.

1) $$\frac{v_o}{e} = \frac{ABk_{cat}}{K_aB + K_bA + AB}$$

2) $$\frac{v_o}{e} = \frac{ABk_{cat}}{K_aB + K_bA(1 + \frac{A}{K_{ia}}) + AB}$$

2.4 Results

2.4.1 Circular Dichroism, Fluorescence Spectroscopy, and UV-Visible Absorption Spectroscopy with NQO-P78G

After NQO-P78G was expressed and purified to high levels following the same protocol as previously described for NQO-WT, the mutant enzyme was investigated using various

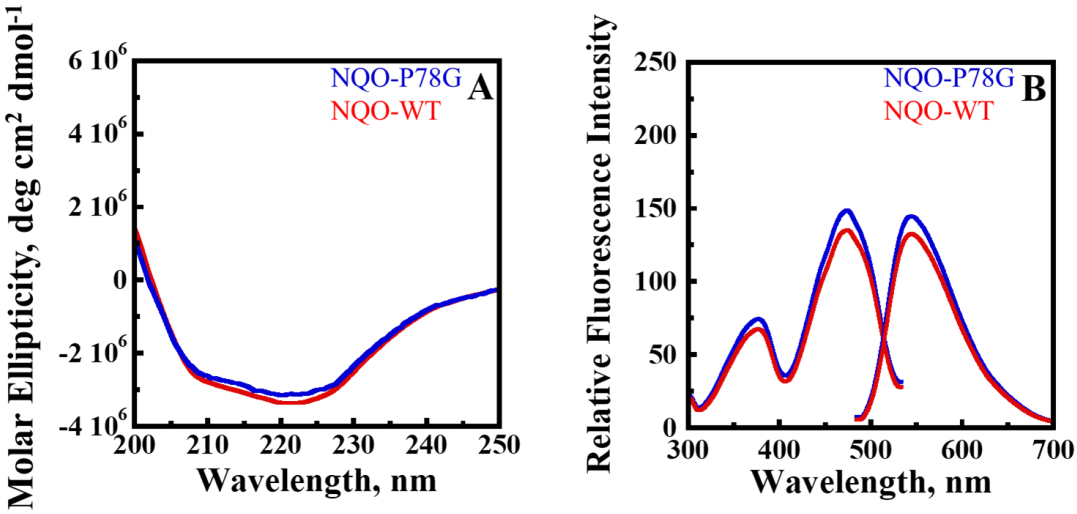

Figure 2.2. Circular Dichroism and Fluorescence Spectra of NQO-P78G and NQO-WT. *(A) CD spectra of NQO-P78G (blue) and NQO-WT (red) were determined in 20 mM potassium phosphate, pH 7.0, and 200 mM sodium chloride at 25 °C. The far-UV CD spectra were measured from 200 – 250 nm with a single scan at a scan speed of 20 nm/min, data pitch of 0.5 nm, and D.I.T of 0.5 s. Data were analyzed and smoothed by the Means-Movement method, using Jasco Spectra Analysis software. (B) Fluorescence excitation and emissions peaks for NQO-P78G (blue) and NQO-WT (red) were acquired in 20 mM potassium pyrophosphate, pH 6.0, and 200 mM sodium chloride at 15 °C. Enzymes were concentrated to 3 μM before measurements were taken. Spectra ranging from 300 – 530 nm represent the excitation spectra, while spectra ranging from 500 – 700 nm represent emission spectra.*

spectroscopic techniques to determine if the mutation altered the biophysical properties of NQO in solution. Circular dichroism (CD), fluorescence spectroscopy, and UV-visible absorption spectroscopy were utilized to probe the biophysical properties of NQO-P78G and compare them to those of NQO-WT. The use of spectroscopic techniques allowed for a thorough analysis of the secondary structure elements and active site environment in NQO-P78G to establish if the mutation altered the structural properties of NQO.

The far-UV CD spectrum for NQO-P78G was solved and compared to that of NQO-WT to determine if the P78G mutation altered the secondary structure elements characteristic of NQO. Far-UV CD spectra were recorded from 200 to 250 nm at pH 7.0 and 25 °C to ensure the high concentration of salt necessary to prevent NQO from crashing out of solution did not affect the CD signal. Figure 2.2A shows the CD spectrum for NQO-P78G is almost identical to that of NQO-WT at the far-UV region, suggesting that the P78G mutation minimally affected the secondary

structure elements in NQO. The results suggest the folding of the secondary structures that form the TIM-barrel and extended domains in NQO were unaffected by the P78 to glycine mutation allowing for subsequent experiments to occur without worrying if the mutant's secondary structures were properly folded in solution.

The fluorescence spectrum of the flavin bound to NQO-P78G was determined compared to those of NQO-WT to probe whether the replacement of P78 with glycine altered the active site microenvironment surrounding the flavin. Upon exciting NQO-P78G at 474 nm, a single emission band with a maximum at 544 nm was observed at pH 6.0 (**Fig. 2.2B**). When the emission wavelength was set at 544 nm, the excitation scan of NQO-P78G yielded two peaks with maxima at 377 and 474 nm (**Fig. 2.2B**). For comparison, the emission maximum of NQO-WT was determined at 545 nm, and the excitation peaks at 377 and 474 nm at pH 6.0 (**Fig. 2.2B**). A comparison between the fluorescence peaks of NQO-P78G and NQO-WT at pH 6.0 determined the P78G mutation had a minimal effect on the relative fluorescence intensities with no effect on peak wavelengths.

The UV-visible absorption spectrum of NQO-P78G was monitored as a function of pH and compared to that of NQO-WT to investigate further if the P78G mutation altered the active site microenvironment surrounding the flavin. The absorption spectrum for NQO-P78G revealed two excitation peaks characteristic of oxidized flavoproteins at 370 and 461 nm at pH 8.0 (**Fig 2.3A**). As pH increased from 8.0 to 11.5, the absorption spectrum of NQO-P78G was minimally affected where a ≤ 2% change in absorption intensities and a ≤ 5 nm difference in peak wavelengths was observed for both peaks. The absorption spectrum for NQO-WT was determined and compared to NQO-P78G, which revealed changes by ≤ 15% in the intensity of the 370 nm peak, ≤ 4% in the intensity of the 461 nm peak, and ≤ 5 nm in the wavelengths of both oxidized peaks from pH 8.0

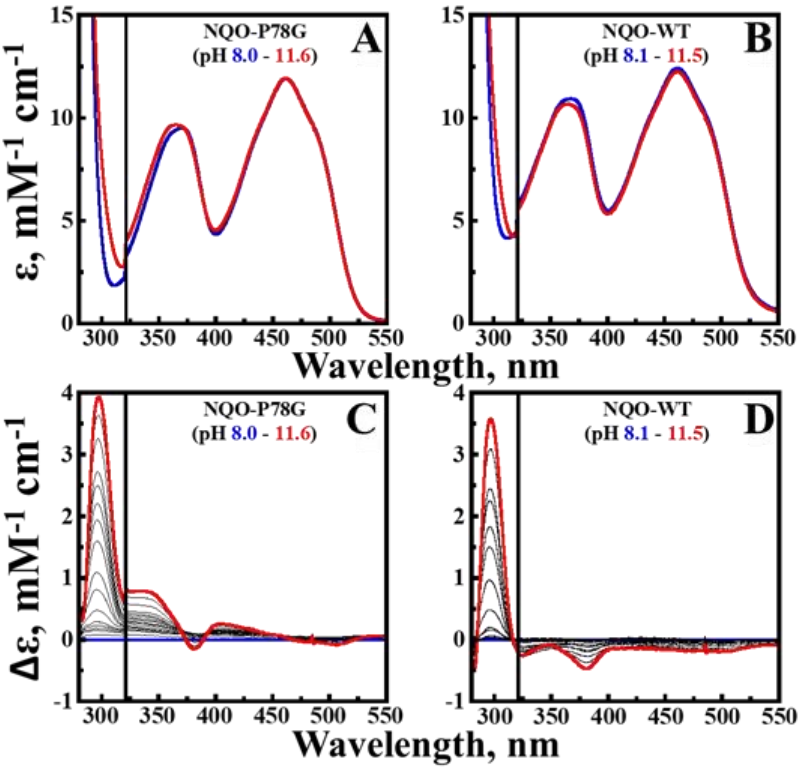

Figure 2.3. Effects of pH on the Absorption Spectra of NQO-P78G and NQO-WT.
Absorption spectra for (A) NQO-P78G and (B) NQO-WT are shown as pH increases from 8.0 (blue) to 11.5 (red). Difference absorption spectra for (C) NQO-P78G and (D) NQO-WT are shown with the same color coding as in panel A and B, where the spectra at pH 8.0 is used as a baseline. Extinction coefficient values were corrected for the protein absorption (≥320 nm) by adjusting for flavin binding. The FMN/enzyme stoichiometry is 0.7 for NQO-P78G and 0.8 for NQO-WT. Spectra were recorded in 10 mM sodium phosphate, 10 mM sodium pyrophosphate, pH 8.0, 10 mM sodium chloride, and 20% glycerol at 15 °C.

to 11.5 (**Fig 2.3B**). The largest spectral changes resulting from an increase in pH were seen at 297 nm, where a maximal increase of 3.9 and 3.6 $mM^{-1}cm^{-1}$ was determined for NQO-P78G and NQO-WT, respectively (**Fig 2.3CD**). Previous studies demonstrated that spectral changes at 297 nm are associated with the deprotonation of tyrosine residues located throughout the enzyme; thus, changes at this wavelength do not necessarily probe the flavin's environment in NQO.[93-95] In contrast, the 320-500 nm region of flavin's absorption spectrum is commonly used to investigate the active site environment of flavoproteins.[96, 97] The difference absorption spectra for NQO-P78G and NQO-WT demonstrated a ≤ 1 $mM^{-1}cm^{-1}$ change in the 320-500 nm region, suggesting the

active site environment surrounding the flavin cofactor in NQO was minimally affected by pH and the P78G mutation (**Fig. 2.3CD**).

2.4.2 Backbone Dynamics of NQO-P78G

Molecular dynamic (MD) simulations were performed on (i) NQO-P78G, (ii) NQO-WT, (iii) NQO-P78G with bound NAD^+, and (iv) NQO-WT with bound NAD^+ where the resulting trajectories were compared to investigate how the replacement of P78 with glycine altered the

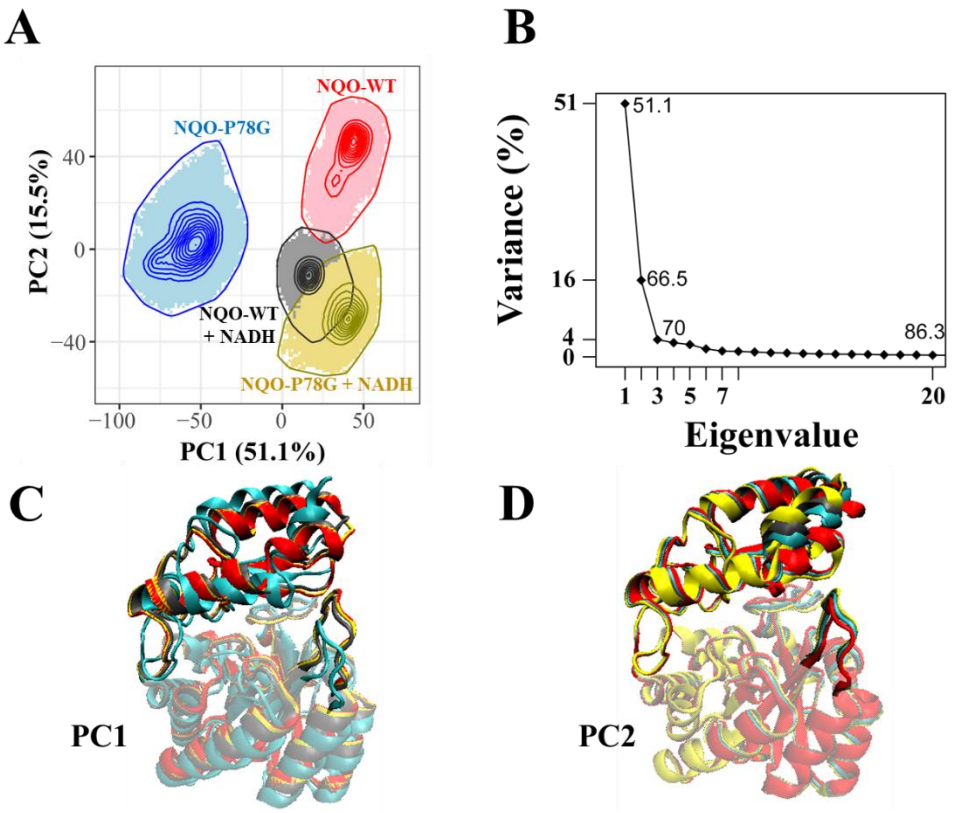

Figure 2.4. PCA of the Cartesian Coordinates of Heavy Backbone Atoms from NQO Simulations.
(A) The PCA plot depicts the conformations of NQO-P78G (blue), NQO-WT (red), NQO-P78G with bound NAD^+ (yellow), and NQO-WT with bound NAD^+ (grey) along the first two principal components (PC1 and PC2), which captures the most significant structural variance between the systems. The number in the axis label indicates the percent variance captured by the corresponding PC. Shaded regions indicate conformations an enzyme system can take, while contour lines represent probability density distributions of each production's conformational states. (B) The scree plot measures the compounded percent total variance captured as a function of eigenvalue ranks or principal components. For example, the first principal component captures 51% of the total variance, while the first 20 principal components capture 86% of the total variance. The most probable backbone conformation for all four systems is shown at (C) PC1 and (D) PC2 where colors represent the same systems as described in panel A.

preferred conformational states of the gate in NQO. Protein backbone conformations were sampled from the four MD simulation productions, and the top two principal components (PC1 and PC2) were computed using principal component analysis (PCA). All four simulation trajectories with NQO sampled a well-defined conformational space at PC1 and PC2, demonstrating that the backbone dynamics used for the PCA represent localized conformations after the dynamics equilibrated (**Fig 2.4A**). A scree-plot analysis established that PC1 and PC2 capture 67% of the total structural variance between all four systems, which represents the dominant collective motions from the PCA (**Fig 2.4B**). The PCA plot demonstrated that NQO-P78G and NQO-WT in the ligand-free form do not overlap at the conformational space described by PC1. In contrast, a significant overlap in conformational states between NQO-P78G with bound NAD^+ and NQO-WT with bound NAD^+ is observed at PC1 and PC2, suggesting that the P78G mutation altered the dynamics of NQO in the ligand-free form with a minimal effect on the dynamics of NQO in the ligand-bound form. A comparison of the conformational space sampled by all four simulations at PC1 and PC2 revealed NQO-P78G in the ligand-free form is the only system to differ along PC1, indicating that the motions along PC1 illustrate the effect of a P78G mutation on the backbone dynamics of NQO (**Fig 2.4A**).

The most probable conformational state for each simulation at PC1 or PC2 was projected onto the backbone of NQO to visualize how the P78G mutation altered the preferred conformational state of the secondary and tertiary structures in ligand-free NQO. The PC1 projection visualizes conformational variation throughout the entire backbone of NQO, where the largest deviations are observed at loop 3 of the TIM-barrel domain and the entirety of the extended domain (**Fig 2.4C**). In contrast, the PC2 projection only depicts structural variation in NQO surrounding an α-helix in the extended domain, known as the interrupted helix, that appears to be

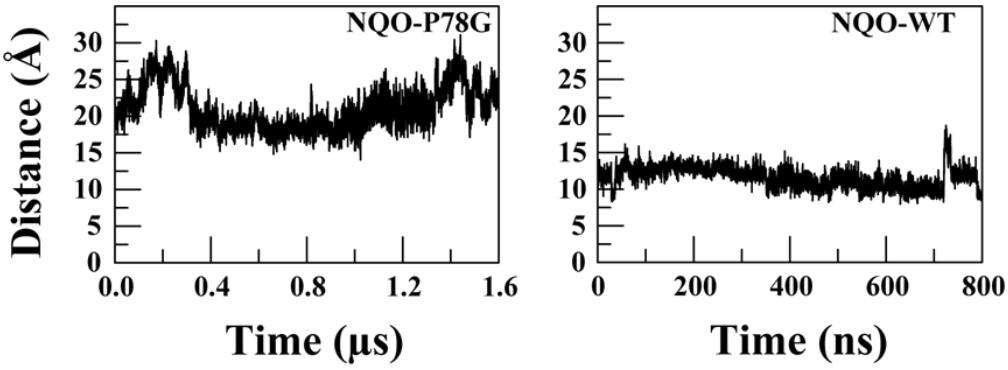

Figure 2.5. Separation between Q80 and Y261 in NQO-P78G.
The distance between the Cα atoms of Q80 and Y261 is shown as a function of time for NQO-P78G and NQO-WT. The separation was measured over simulation times where the backbone dynamics for each system were equilibrated.

slightly unwound (**Fig 2.4D**). Principal component projections presented here demonstrate that loop 3 and the extended domain extend away from one another in ligand-free NQO-P78G to open up the gate region of NQO, which exposes the active site to the environment surrounding the enzyme.

The separation between loop 3 and the extended domain in NQO-P78G was assessed and compared to that of NQO-WT to investigate how the P78G mutation altered the fluctuations of the gate. The distance between the Cα atoms of Q80 located on loop 3 and Y261 located near the interrupted helix was used to probe the gate's dynamics. The separation between the gate residues Q80 and Y261 was chosen to illustrate gate dynamics because the crystal structures of NQO suggest a hydrogen bond forms between the two residues in the ligand-bound conformation of the enzyme, which stabilizes the enzyme-substrate complex. The backbone dynamics in NQO-P78G indicated that Q80 and Y261 fluctuate between 15 and 30 Å from one another (**Fig 2.5**). For comparison, the distance between Q80 and Y261 was determined in NQO-WT, which demonstrated a separation ranging from 8 to 20 Å between the two gate residues (**Fig 2.5)**. The results presented here suggest gate conformations in NQO-P78G can sample a separation between

loop 3 and the extended domain that is 10 Å wider than the maximum displacement of the gate in NQO-WT.

2.4.3 Difference Community Network Analysis

Differences in the residue-residue communication pathways between NQO-P78G and NQO-WT were determined to investigate how the P78G mutation altered residue contacts within the gate region of NQO. The contact probability of long-range residue communications was calculated and compared between the mutant and wild-type enzymes in the ligand-free form where only significant contact changes (changes with an absolute probability difference ≥ 0.1) were

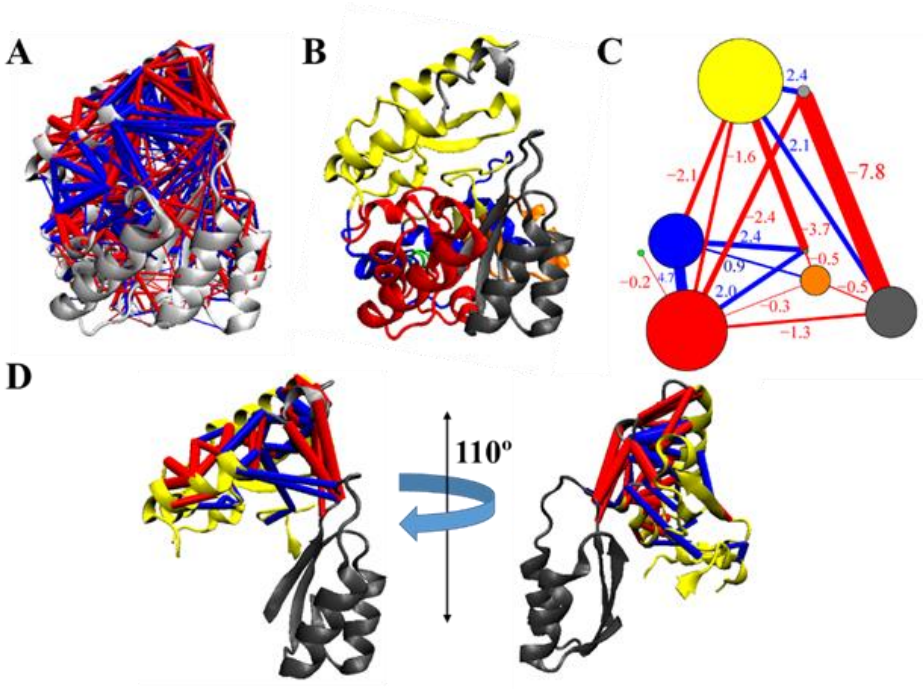

Figure 2.6. Alterations in the Residue-Residue Communication Pathway by NQO-P78G.
(A) The probability of residue-residue contact changes (df) from NQO-WT to NQO-P78G is mapped onto the backbone of NQO. Contacts that form are depicted as blue cylinders, whereas contacts that break are depicted as red cylinders with a cylindric radius proportional to |df|. Contacts are shown if they are meaningful (i.e., |df| ≥ 0.1). (B) The 8 consensus communities identified by the dCNA are color-coded onto the backbone of NQO. (C) Residue contact changes obtained in panel A were mapped onto the community partition obtained by dCNA. Communities are represented by vertices that have the same color as in panel B. The radius of the vertices is proportional to the number of residues in that community, whereas the red and blue lines linking the communities represent the net contact probability difference between two communities. (D) Residue-residue contacts with a |df| ≥ 0.5 were mapped onto the backbone of NQO containing only the grey, silver, and yellow communities to illustrate the interactions between loop 3 and the extended domain.

assessed (**Fig. 2.6A**). The contact analysis revealed the P78G mutation both broke and formed contacts throughout the entire structure of NQO. A difference contact network analysis (dCNA) was performed to describe the residue contact changes resulting from the P78G mutation in a simplified format. A total of 8 consensus communities were defined by dCNA where each community represents a structural portion of NQO whose residues are more densely connected by stable contacts compared to contacts between other communities (**Fig. 2.6B**). The TIM-barrel and extended domains were divided into multiple communities by dCNA where the grey community contains loop 3, the silver community contains the interrupted helix, and the yellow community contains the extended domain and loop 6 of NQO (**Fig. 2.6B**). The total contact changes between each community were calculated and presented in a two-dimensional diagram to determine if the P78G mutation ultimately stabilized or destabilized contacts among structural portions of NQO (**Fig. 2.6C**). The largest contact change in the communication pathway of NQO-P78G occurred between the grey and silver communities, where a local contact breakage with a probability difference of -7.8 was identified (**Fig. 2.6C**). Contact changes with an absolute probability difference ≥ 0.5 were mapped onto the grey, silver, and yellow communities at the specific residues they occur on, which demonstrated that significant contact breakages formed by the P78G mutation occurred between the protein backbone surrounding residue 78 and the interrupted helix of the extended domain (**Fig. 2.6D**). Visualizing the significant contact breakages between the region of loop 3 surrounding the site of the P78G mutation and the interrupted helix of the extended domain supports the PCA, which suggests the active site is more open to the bulk solvent in NQO-P78G.

2.4.4 Steady-State Kinetics of NQO-P78G.

The steady-state kinetic parameters of NQO-P78G were determined and compared to those of NQO-WT to investigate how the gate's altered dynamics affected the rate of substrate binding and turnover in NQO. The preferred oxidizing substrate for NQO, benzoquinone, resulted in substrate inhibition with NQO-P78G; thus, Coenzyme-Q_0 (CoQ_0) was utilized as the oxidizing substrate at pH 6.0 to determine the kinetic parameters of the mutant.[54] In contrast, the optimal conditions used to probe the kinetic parameters for NQO-P78G resulted in substrate inhibition by NADH in NQO-WT. As a result, values for the kinetic parameters K_{NADH} and k_{cat}/K_{NADH} could not be determined for the wild-type enzyme; thus, the kinetic comparison between NQO-P78G and NQO-WT focused on changes in the k_{cat}, K_{CoQ0}, and k_{cat}/K_{CoQ0} values. The best fits for both enzymes' kinetic parameters were obtained using an equation describing a ping-pong bi-bi steady-state mechanism, suggesting the P78G mutation did not alter the mechanism NQO utilizes to turnover (**Table 1**). A comparison of the measured kinetic parameters demonstrates 3.5-fold

Table 2.1. Steady-State Kinetic Parameters of NQO-WT and NQO-P78G with CoQ_0 and NADH as Substrates

Kinetic Parameter	NQO-WT	NQO-P78G
k_{cat}, s^{-1}	11 ± 1	5.4 ± 0.2
K_{NADH}, μM	ND[α]	130 ± 10
K_{CoQ0}, μM	35 ± 6	10 ± 1
$K_{i,\ NADH}$, μM	1.1 ± 0.1	NULL[β]
k_{cat} / K_{NADH}, $M^{-1}s^{-1}$	ND[α]	43,000 ± 3,000
k_{cat} / K_{CoQ0}, $M^{-1}s^{-1}$	320,000 ± 57,000	560,000 ± 46,000
R^2	0.990	0.988

Summary of steady-state kinetic parameters for NQO-WT and NQO-P78G. Enzymes were tested in 20 mM potassium phosphate, pH 6.0, and 100 mM sodium chloride at 25 °C. Steady-state kinetic parameters were measured by following the reduction of NADH using the extinction coefficient value ε_{340} = 6,220 $M^{-1}cm^{-1}$.

[α]Values were unable to be determined due to substrate inhibition by NADH.

[β]Value was not determined as it was not a kinetic parameter relevant to the mechanism studied.

decrease in the K_{CoQ0} value, a 2.0-fold decrease in the k_{cat} value, and a 1.8-fold increase in the k_{cat}/K_{CoQ0} value from NQO-WT to NQO-P78G.

2.5 Discussion

Previous crystallographic studies on NQO with and without bound NAD^+ suggest loop 3 adopts open and closed conformations, which function to secure substrates in the enzyme's active site pocket.[58] The mutagenic, spectroscopic, computational, and kinetic study presented here demonstrates that a loss in rigidity at loop 3 by a P78G mutation alters the dynamics of the loop in the ligand-free form to expose the active site to the bulk solvent while minimally affecting the structural, biophysical, and mechanistic properties of NQO. Furthermore, the P78G mutation altered the dynamics of loop 3 and the extended domain, suggesting the domain is also capable of sampling open and closed conformations that coincide with the loop to form the gate and bind substrates in NQO.

The P78G mutation on βα loop 3 had a minimal effect on the structural and biophysical properties characteristic of the protein and flavin cofactor in NQO. Evidence to support this conclusion comes from comparing the CD, fluorescence, and UV-visible absorption spectra of NQO-P78G to NQO-WT. CD determined the mutant and wild-type enzymes had far-UV spectra that were virtually identical, indicating minimal differences in the secondary structure elements between the two enzymes in solution. Changes in an enzyme's secondary structure elements are commonly monitored using CD to determine if perturbations in an enzyme's structure or environment will unfold the enzyme.[98] The lack of a large effect on the secondary structure elements of NQO by the P78G mutation is consistent with a minimal change in the folding of NQO, which supports previous TIM-barrel studies that suggest mutations on βα loops do not jeopardize an enzyme's stability.[63] Furthermore, the protein environment surrounding the flavin

cofactor was minimally altered by replacing P78 with a glycine, as demonstrated by the fluorescence and UV-visible absorption spectra of the mutant and wild-type enzymes, which showed slight differences in absorption wavelength and intensity.[99-103]

The dynamics of the gate in the ligand-free form of NQO-P78G sampled more open conformations compared to the wild-type enzyme, which exposes the active site of NQO to the environment surrounding the protein. Evidence to support this conclusion comes from the molecular dynamics and subsequent protein backbone investigations with NQO-P78G and NQO-WT in the ligand-free form. The most significant variation in enzyme conformations following the P78G mutation was observed at loop 3 and, unexpectedly, the extended domain where the two subunits extended away from one another to open the gate region of NQO. The separation between loop 3 and the extended domain was investigated by monitoring the distance between Q80 and Y261 over time, which demonstrated the gate in NQO-P78G can sample a conformation that is 10 Å more open than the maximum displacement of the gate in NQO-WT. The synchronous displacement of loop 3 and the extended domain in the mutant enzyme suggests that gate conformations in NQO are not modulated by the displacement of loop 3 alone, as previously hypothesized by crystal structures of NQO. Instead, molecular dynamics with NQO suggest gate conformations are modulated by the associated dynamics of loop 3 and the extended domain.

Decreasing the rigidity at loop 3 by replacing P78 with a glycine breaks residue-residue contacts between loop 3 and extended domain in NQO. Evidence to support this conclusion comes from the dCNA of NQO-P78G and NQO-WT in the ligand-free form. Differences in community contacts between the mutant and wild-type enzymes revealed the most significant contact breakages occurred between the portion of the TIM-barrel domain surrounding loop 3 and the interrupted helix with a contact probability difference of – 7.8. Upon further inspection, the dCNA

revealed the significant contact breakages by the P78G mutation formed between the backbone surrounding P78 and residues surrounding Y261 at the interrupted helix in NQO. The results presented here support the backbone trajectory analysis, which suggests the P78G mutation samples more open conformations at the gate in NQO by demonstrating the mutation breaks domain-domain interactions.

NQO-P78G must undergo larger conformational changes throughout the entire protein structure to sample the conformations of the enzyme-substrate complex compared to NQO-WT. Evidence to support this conclusion comes from the PCA with NQO-P78G and NQO-WT with NAD^+ bound and in the ligand-free form. Backbone conformations of the mutant and wild-type enzymes with bound NAD^+ lacked significant differences, demonstrating the dynamics of the enzyme-substrate complex were mostly unaffected by the P78G mutation. The dynamics of the TIM-barrel and extended domains revealed there is no overlap in the conformational states of the protein backbone between NQO-P78G in the ligand-free form and the enzyme-substrate complex of NQO. In contrast, the preferred conformational states of NQO-WT in the ligand-free form contained significant overlap with the dynamics of the enzyme-substrate complex, where only variations at the interrupted helix were observed. The results presented here suggest the P78G mutation would perturb the turnover of NQO at the substrate binding step as NQO-P78G must undergo larger conformational changes to form the enzyme-substrate complex and proceed through catalysis.

Replacement of P78 with glycine had a small yet notable effect on the rate of association of the oxidized quinone with the reduced enzyme to form the enzyme-quinone complexes that partition forward to catalysis. Evidence to support this conclusion comes from the steady-state kinetic parameters for NQO-P78G, and NQO-WT determined with NADH and CoQ_0 as substrates.

A twofold increase in the k_{cat}/K_{CoQ0} value was observed in NQO-P78G compared to NQO-WT at pH 6.0. Typically, mutations of conserved residues in enzymes yield lower values for k_{cat}/K_m and k_{cat}[104-106]; thus, the unexpected observed increase in the k_{cat}/K_{CoQ0} value suggests the P78G mutation may have affected substrate capture. The molecular dynamics presented above support this conclusion by demonstrating that the gate in NQO-P78G is more open than NQO-WT in the ligand-free form, which may allow the CoQ_0 substrate to more easily enter the active site pocket to form the enzyme-quinone complex. However, the magnitude of the effect on k_{cat}/K_{CoQ0} is small, indicating that if the P78G mutation altered the rate of association of the oxidized quinone with the enzyme, the change is minimal. The alternative possibility is that the mutation increased the probability the enzyme-quinone complexes partition forward to catalysis by increasing the rate of the two-electron quinone reduction. It is unlikely the P78G mutation results in an increased rate of hydride transfer as molecular dynamics demonstrated the preferred conformations of NQO in the ligand-bound form were not significantly altered by the mutation, which suggests the structure of the mutant enzyme will not perturb the catalytic step in NQO.

2.6 Conclusions

In summary, the results presented here demonstrate a decrease in the structural rigidity at loop 3 by a P78G mutation results in more open conformations of the gate in the substrate-free form of NQO, which does not significantly alter the active site environment or steady-state kinetic parameters of the enzyme. The molecular dynamics of NQO-P78G presented here build upon previous crystal structure studies with NQO by demonstrating gate conformations are modulated through dynamic motions at loop 3 and the extended domain. Interestingly, the current classification scheme for gates in enzymes has not yet identified a gate that consists of a loop and a domain that fluctuate in a concerted fashion; thus, we provide an extension to the classification

scheme pertaining to the study of enzyme gates as the gate of NQO contains structural features belonging to two different classes of gates. Future structural studies on enzymes involving gates should consider the possibility that gating loops may require dynamic motions from neighboring domains to function properly.

Gates in enzymes offer a promising site to engineer catalytic functions through site-directed mutations, replacements, or deletions. The current study provides a detailed investigation of the relationship between gate rigidity and enzyme turnover in NQO, which should be considered during the *de novo* synthesis of gate-containing enzymes. Surprisingly, the wider conformations sampled by the gate in the ligand-free form of NQO-P78G were determined to have a minimal to no effect on the rate of substrate capture in NQO. However, the *de novo* synthesis of enzymes commonly employs multiple point mutations to reengineer catalytic functions as a single point mutation is unlikely to increase enzymatic efficiencies significantly. Future studies on the *de novo* synthesis of gate-containing enzymes should consider widening the conformations of the gate through a point mutation similar or identical to the P78G mutation presented here, as the present study suggests this may contribute to an increase in the rate of substrate capture.

2.7 References

[1] Karplus, M., and Kuriyan, J. (2005) Molecular dynamics and protein function, *Proc. Natl. Acad. Sci. U.S.A. 102*, 6679.

[2] Gora, A., Brezovsky, J., and Damborsky, J. (2013) Gates of Enzymes, *Chem. Rev. 113*, 5871-5923.

[3] Papaleo, E., Saladino, G., Lambrughi, M., Lindorff-Larsen, K., Gervasio, F. L., and Nussinov, R. (2016) The Role of Protein Loops and Linkers in Conformational Dynamics and Allostery, *Chem. Rev. 116*, 6391-6423.

[4] Gerstein, M., Lesk, A. M., and Chothia, C. (1994) Structural mechanisms for domain movements in proteins, *Biochemistry 33*, 6739-6749.

[5] Zhu, X., Clarke, R., Puppala, A. K., Chittori, S., Merk, A., Merrill, B. J., Simonović, M., and Subramaniam, S. (2019) Cryo-EM structures reveal coordinated domain motions that govern DNA cleavage by Cas9, *Nat. Struc. Mol. Biol. 26*, 679-685.

[6] Müller, C. W., Schlauderer, G. J., Reinstein, J., and Schulz, G. E. (1996) Adenylate kinase motions during catalysis: an energetic counterweight balancing substrate binding, *Structure 4*, 147-156.

[7] Munro, A. W., Leys, D. G., McLean, K. J., Marshall, K. R., Ost, T. W. B., Daff, S., Miles, C. S., Chapman, S. K., Lysek, D. A., Moser, C. C., Page, C. C., and Dutton, P. L. (2002) P450 BM3: the very model of a modern flavocytochrome, *Trends Biochem. Sci. 27*, 250-257.

[8] Xiang, J., Jung, J.-y., and Sampson, N. S. (2004) Entropy effects on protein hinges: the reaction catalyzed by triosephosphate isomerase, *Biochemistry 43*, 11436-11445.

[9] Barbe, S., Cortés, J., Siméon, T., Monsan, P., Remaud-Siméon, M., and André, I. (2011) A mixed molecular modeling-robotics approach to investigate lipase large molecular motions, *Proteins 79*, 2517-2529.

[10] Gunasekaran, K., and Nussinov, R. (2004) Modulating Functional Loop Movements: The Role of Highly Conserved Residues in the Correlated Loop Motions, *Chem. Bio. Chem. 5*, 224-230.

[11] Ouedraogo, D., Souffrant, M., Vasquez, S., Hamelberg, D., and Gadda, G. (2017) Importance of Loop L1 Dynamics for Substrate Capture and Catalysis in *Pseudomonas aeruginosa* d-Arginine Dehydrogenase, *Biochemistry 56*, 2477-2487.

[12] Pasi, M., Riccardi, L., Fantucci, P., De Gioia, L., and Papaleo, E. (2009) Dynamic properties of a psychrophilic α-amylase in comparison with a mesophilic homologue, *J. Phys. Chem. B 113*, 13585-13595.

[13] Zhou, H.-X., Wlodek, S. T., and McCammon, J. A. (1998) Conformation gating as a mechanism for enzyme specificity, *Proc. Natl. Acad. Sci. U.S.A. 95*, 9280-9283.

[14] Son, S.-Y., Ma, J., Kondou, Y., Yoshimura, M., Yamashita, E., and Tsukihara, T. (2008) Structure of human monoamine oxidase A at 2.2-Å resolution: the control of opening the entry for substrates/inhibitors, *Proc. Natl. Acad. Sci. U.S.A. 105*, 5739-5744.

[15] Ma, B., Tsai, C.-J., Haliloğlu, T., and Nussinov, R. (2011) Dynamic Allostery: Linkers Are Not Merely Flexible, *Structure 19*, 907-917.

[16] Cui, Q., and Karplus, M. (2008) Allostery and cooperativity revisited, *Protein Sci. 17*, 1295-1307.

[17] Masterson, L. R., Shi, L., Metcalfe, E., Gao, J., Taylor, S. S., and Veglia, G. (2011) Dynamically committed, uncommitted, and quenched states encoded in protein kinase A revealed by NMR spectroscopy, *Proc. Natl. Acad. Sci. U.S.A. 108*, 6969.

[18] Haliloglu, T., and Bahar, I. (2015) Adaptability of protein structures to enable functional interactions and evolutionary implications, *Curr. Opin. Struct. Biol. 35*, 17-23.

[19] Bahar, I., Chennubhotla, C., and Tobi, D. (2007) Intrinsic dynamics of enzymes in the unbound state and relation to allosteric regulation, *Curr. Opin. Struct. Biol. 17*, 633-640.

[20] Zhang, Y., Doruker, P., Kaynak, B., Zhang, S., Krieger, J., Li, H., and Bahar, I. (2020) Intrinsic dynamics is evolutionarily optimized to enable allosteric behavior, *Curr. Opin. Struct. Biol. 62*, 14-21.

[21] Henzler-Wildman, K. A., Thai, V., Lei, M., Ott, M., Wolf-Watz, M., Fenn, T., Pozharski, E., Wilson, M. A., Petsko, G. A., Karplus, M., Hübner, C. G., and Kern, D. (2007) Intrinsic motions along an enzymatic reaction trajectory, *Nature 450*, 838-844.

[22] Kar, G., Keskin, O., Gursoy, A., and Nussinov, R. (2010) Allostery and population shift in drug discovery, *Curr. Opin. Pharma.10*, 715-722.

[23] Nussinov, R., and Tsai, C.-J. (2013) Allostery in Disease and in Drug Discovery, *Cell 153*, 293-305.

[24] Fang, Z., Grütter, C., and Rauh, D. (2013) Strategies for the Selective Regulation of Kinases with Allosteric Modulators: Exploiting Exclusive Structural Features, *ACS Chem. Biol. 8*, 58-70.

[25] Lu, S., Ji, M., Ni, D., and Zhang, J. (2018) Discovery of hidden allosteric sites as novel targets for allosteric drug design, *Drug Discov. Today 23*, 359-365.

[26] Lu, S., Qiu, Y., Ni, D., He, X., Pu, J., and Zhang, J. (2020) Emergence of allosteric drug-resistance mutations: new challenges for allosteric drug discovery, *Drug Discov. Today 25*, 177-184.

[27] Nanda, V., and Koder, R. L. (2010) Designing artificial enzymes by intuition and computation, *Nature Chem. 2*, 15-24.

[28] France, S. P., Hepworth, L. J., Turner, N. J., and Flitsch, S. L. (2017) Constructing Biocatalytic Cascades: *In Vitro* and *in Vivo* Approaches to de Novo Multi-Enzyme Pathways, *ACS Catal. 7*, 710-724.

[29] Röthlisberger, D., Khersonsky, O., Wollacott, A. M., Jiang, L., DeChancie, J., Betker, J., Gallaher, J. L., Althoff, E. A., Zanghellini, A., Dym, O., Albeck, S., Houk, K. N., Tawfik, D. S., and Baker, D. (2008) Kemp elimination catalysts by computational enzyme design, *Nature 453*, 190-195.

[30] Basanta, B., Bick, M. J., Bera, A. K., Norn, C., Chow, C. M., Carter, L. P., Goreshnik, I., Dimaio, F., and Baker, D. (2020) An enumerative algorithm for *de novo* design of proteins with diverse pocket structures, *Proc. Natl. Acad. Sci. U.S.A. 117*, 22135.

[31] Henzler-Wildman, K., and Kern, D. (2007) Dynamic personalities of proteins, *Nature 450,* 964-972.

[32] Schwartz, S. D., and Schramm, V. L. (2009) Enzymatic transition states and dynamic motion in barrier crossing, *Nat. Chem. Biol. 5*, 551-558.

[33] Kamerlin, S. C. L., and Warshel, A. (2010) At the dawn of the 21st century: Is dynamics the missing link for understanding enzyme catalysis?, *Proteins 78,* 1339-1375.

[34] Richard, J. P. (2019) Protein Flexibility and Stiffness Enable Efficient Enzymatic Catalysis, *J. Am. Chem. Soc. 141*, 3320-3331.

[35] Marques, S. M., Daniel, L., Buryska, T., Prokop, Z., Brezovsky, J., and Damborsky, J. (2017) Enzyme Tunnels and Gates As Relevant Targets in Drug Design, *Med. Res. Rev. 37,* 1095-1139.

[36] Ko, T.-P., Chen, Y.-K., Robinson, H., Tsai, P.-C., Gao, Y.-G., Chen, A. P. C., Wang, A. H. J., and Liang, P.-H. (2001) Mechanism of Product Chain Length Determination and the Role of a Flexible Loop in *Escherichia coli* Undecaprenyl-pyrophosphate Synthase Catalysis, *J. Biol. Chem. 276*, 47474-47482.

[37] Kotik, M., Štěpánek, V., Kyslík, P., and Marešová, H. (2007) Cloning of an epoxide hydrolase-encoding gene from *Aspergillus niger* M200, overexpression in *E. coli*, and modification of activity and enantioselectivity of the enzyme by protein engineering, *J. Biotechnol. 132*, 8-15.

[38] Xin, Y., Gadda, G., and Hamelberg, D. (2009) The Cluster of Hydrophobic Residues Controls the Entrance to the Active Site of Choline Oxidase, *Biochemistry 48*, 9599-9605.

[39] Cojocaru, V., Winn, P. J., and Wade, R. C. (2007) The ins and outs of cytochrome P450s, *Biochim. Biophys. Acta Gen. Subj. 1770*, 390-401.

[40] Fan, Y., Lund, L., Shao, Q., Gao, Y.-Q., and Raushel, F. M. (2009) A Combined Theoretical and Experimental Study of the Ammonia Tunnel in Carbamoyl Phosphate Synthetase, *J. Am. Chem. Soc. 131*, 10211-10219.

[41] Couture, J.-F., Legrand, P., Cantin, L., Labrie, F., Luu-The, V., and Breton, R. (2004) Loop Relaxation, A Mechanism that Explains the Reduced Specificity of Rabbit 20α-Hydroxysteroid Dehydrogenase, A Member of the Aldo-Keto Reductase Superfamily, *J. Mol. Biol. 339*, 89-102.

[42] Rout, M. K., Lee, B. L., Lin, A., Xiao, W., and Spyracopoulos, L. (2018) Active Site Gate Dynamics Modulate the Catalytic Activity of the Ubiquitination Enzyme E2-25K, *Sci. Rep. 8*, 7002.

[43] Zawaira, A., Coulson, L., Gallotta, M., Karimanzira, O., and Blackburn, J. (2011) On the deduction and analysis of singlet and two-state gating-models from the static structures of mammalian CYP450, *J. Struct. Biol.173*, 282-293.

[44] Nestl, B. M., and Hauer, B. (2014) Engineering of Flexible Loops in Enzymes, *ACS Catal. 4*, 3201-3211.

[45] Khan, F. I., Lan, D., Durrani, R., Huan, W., Zhao, Z., and Wang, Y. (2017) The Lid Domain in Lipases: Structural and Functional Determinant of Enzymatic Properties, *Front. Bioeng. Biotechnol. 5*, 16.

[46] Vardar, G., and Wood, T. K. (2005) Alpha-Subunit Positions Methionine 180 and Glutamate 214 of *Pseudomonas stutzerin* OX1 Toluene-Xylene Monooxygenase Influence Catalysis, *J. Bacteriol.187*, 1511.

[47] Yu, X.-W., Zhu, S.-S., Xiao, R., and Xu, Y. (2014) Conversion of a *Rhizopus chinensis* lipase into an esterase by lid swapping, *J. Lipid Res. 55*, 1044-1051.

[48] Gao, B., Xu, T., Lin, J., Zhang, L., Su, E., Jiang, Z., and Wei, D. (2011) Improving the catalytic activity of lipase LipK107 from Proteus sp. by site-directed mutagenesis in the lid domain based on computer simulation, *J. Mol. Catal. B Enzym. 68*, 286-291.

[49] Lafaquière, V., Barbe, S., Puech-Guenot, S., Guieysse, D., Cortés, J., Monsan, P., Siméon, T., André, I., and Remaud-Siméon, M. (2009) Control of Lipase Enantioselectivity by Engineering the Substrate Binding Site and Access Channel, *Chem. Bio. Chem. 10*, 2760-2771.

[50] Secundo, F., Carrea, G., Tarabiono, C., Brocca, S., and Lotti, M. (2004) Activity and enantioselectivity of wildtype and lid mutated *Candida rugosa* lipase isoform 1 in organic solvents, *Biotechnol. Bioeng. 86,* 236-240.

[51] Yaacob, N., Ahmad Kamarudin, N. H., Leow, A. T. C., Salleh, A. B., Rahman, R. N. Z. R. A., and Ali, M. S. M. (2019) Effects of Lid 1 Mutagenesis on Lid Displacement, Catalytic Performances and Thermostability of Cold-active *Pseudomonas* AMS8 Lipase in Toluene, *Comp. Struct. Biotechnol. J. 17*, 215-228.

[52] Yu, H., Yan, Y., Zhang, C., and Dalby, P. A. (2017) Two strategies to engineer flexible loops for improved enzyme thermostability, *Sci. Rep. 7,* 41212.

[53] Yu, X.-W., Tan, N.-J., Xiao, R., and Xu, Y. (2012) Engineering a Disulfide Bond in the Lid Hinge Region of *Rhizopus chinensis* Lipase: Increased Thermostability and Altered Acyl Chain Length Specificity, *PLOS ONE 7,* e46388.

[54] Ball, J., Salvi, F., and Gadda, G. (2016) Functional Annotation of a Presumed Nitronate Monoxygenase Reveals a New Class of NADH:Quinone Reductases, *J. Biol. Chem. 291*, 21160-21170.

[55] Deller, S., Macheroux, P., and Sollner, S. (2007) Flavin-dependent quinone reductases, *Cell. Mol. Life Sci. 65*, 141.

[56] Iyanagi, T., and Yamazaki, I. (1970) One-electron-transfer reactions in biochemical systems V. Difference in the mechanism of quinone reduction by the NADH dehydrogenase and the NAD(P)H dehydrogenase (DT-diaphorase), *Biochim. Biophys. Acta . Bioenerg. 216,* 282-294.

[57] Lê-Quôc, D., and Lê-Quôc, K. (1989) Relationships between the NAD(P) redox state, fatty acid oxidation, and inner membrane permeability in rat liver mitochondria, *Arch. Biochem. Biophys. 273*, 466-478.

[58] Ball, J., Reis, R. A. G., Agniswamy, J., Weber, I. T., and Gadda, G. (2019) Steric hindrance controls pyridine nucleotide specificity of a flavin-dependent NADH:quinone oxidoreductase, *Protein Sci. 28*, 167-175.

[59] Copley, R. R., and Bork, P. (2000) Homology among (βα)8 barrels: implications for the evolution of metabolic pathways 11 Edited by G. Von Heijne, *J. Mol. Biol. 303*, 627-641.

[60] Gerlt, J. A., and Babbitt, P. C. (2001) Barrels in pieces, *Nat. Struct. Biol. 8*, 5-7.

[61] Wierenga, R. K. (2001) The TIM-barrel fold: a versatile framework for efficient enzymes, *FEBS Lett.492*, 193-198.

[62] Richard, J. P., Amyes, T. L., Goryanova, B., and Zhai, X. (2014) Enzyme architecture: on the importance of being in a protein cage, *Curr. Opin. Chem. Biol. 21*, 1-10.

[63] Höcker, B., Jürgens, C., Wilmanns, M., and Sterner, R. (2001) Stability, catalytic versatility and evolution of the (βα)8-barrel fold, *Curr. Opin. Biotechnol. 12*, 376-381.

[64] Inouye, M. (2016) The first application of site-directed mutagenesis using oligonucleotides for studying the function of a protein, *Gene 593*, 342-343.

[65] Jürgens, C., Strom, A., Wegener, D., Hettwer, S., Wilmanns, M., and Sterner, R. (2000) Directed evolution of a (βα)-barrel enzyme to catalyze related reactions in two different metabolic pathways, *Proc. Natl. Acad. Sci. U.S.A. 97*, 9925.

[66] Petsko, G. A. (2000) Design by necessity, *Nature 403*, 606-607.

[67] Thanki, N., Zeelen, J. P., Mathieu, M., Jaenicke, R., Abagyan, R. A., Wierenga, R. K., and Schliebs, W. (1997) Protein engineering with monomeric triosephosphate isomerase (monoTIM): the modelling and structure verification of a seven-residue loop, *Protein Eng. Des. Sel.10*, 159-167.

[68] Ha, J. Y., Min, J. Y., Lee, S. K., Kim, H. S., Kim, D. J., Kim, K. H., Lee, H. H., Kim, H. K., Yoon, H.-J., and Suh, S. W. (2006) Crystal Structure of 2-Nitropropane Dioxygenase Complexed with FMN and Substrate: Identification of the Catalytic Base *J. Biol. Chem. 281*, 18660-18667.

[69] Inoue, H., Nojima, H., and Okayama, H. (1990) High efficiency transformation of Escherichia coli with plasmids, *Gene 96*, 23-28.

[70] Aliverti, A., Curti, B., and Vanoni, M. A. (1999) Identifying and quantitating FAD and FMN in simple and in iron-sulfur-containing flavoproteins, *Methods Mol. Biol. (Clifton, N.J.) 131*, 9-23.

[71] Whitby, L. G. (1953) A new method for preparing flavin-adenine dinucleotide, *Biochem. J. 54*, 437-442.

[72] Bradford, M. M. (1976) A rapid and sensitive method for the quantitation of microgram quantities of protein utilizing the principle of protein-dye binding, *Anal. Biochem. 72*, 248-254.

[73] Case, D. A., Cerutti, D. S., Cheatham, T. E., III., Darden, T. A., Duke, R. E., Giese, T. J., Gohlke, H., Goetz, A. W., Greene, D., Homeyer, N., Izadi, S., Kovalenko, A., Lee, T. S., LeGrand, S., Li, P., et al. (2016) Amber 2016, *UCSF, CA.*

[74] Maier, J. A., Martinez, C., Kasavajhala, K., Wickstrom, L., Hauser, K. E., and Simmerling, C. (2015) ff14SB: Improving the Accuracy of Protein Side Chain and Backbone Parameters from ff99SB, *J. Chem. Theory Comput. 11*, 3696-3713.

[75] Schneider, C., and Sühnel, J. (1999) A molecular dynamics simulation of the flavin mononucleotide-RNA aptamer complex, *Biopolymers 50*, 287-302.

[76] Jorgensen, W. L., Chandrasekhar, J., Madura, J. D., Impey, R. W., and Klein, M. L. (1983) Comparison of simple potential functions for simulating liquid water, *J. Chem. Phys. 79*, 926-935.

[77] Mark, P., and Nilsson, L. (2001) Structure and Dynamics of the TIP3P, SPC, and SPC/E Water Models at 298 K, *J. Phys. Chem. A 105*, 9954-9960.

[78] Darden, T., York, D., and Pedersen, L. (1993) Particle mesh Ewald: An N·log(N) method for Ewald sums in large systems, *J. Chem. Phys. 98*, 10089-10092.

[79] Ryckaert, J.-P., Ciccotti, G., and Berendsen, H. J. C. (1977) Numerical integration of the cartesian equations of motion of a system with constraints: molecular dynamics of n-alkanes, *J. Chem. Phys. 23*, 327-341.

[80] Roe, D. R., and Cheatham, T. E. (2013) PTRAJ and CPPTRAJ: Software for Processing and Analysis of Molecular Dynamics Trajectory Data, *J. Chem. Theory Comput. 9*, 3084-3095.

[81] Wickham, H. (2016) ggplot2: Elegant Graphics for Data Analysis. 2nd ed., *Springer-Verlag*.

[82] Humphrey, W., Dalke, A., and Schulten, K. (1996) VMD: Visual molecular dynamics, *J. Mol. Graph. 14*, 33-38.

[83] Grant, B. J., Rodrigues, A. P. C., ElSawy, K. M., McCammon, J. A., and Caves, L. S. D. (2006) Bio3d: an R package for the comparative analysis of protein structures, *J. Bioinform. 22*, 2695-2696.

[84] Skjærven, L., Yao, X.-Q., Scarabelli, G., and Grant, B. J. (2014) Integrating protein structural dynamics and evolutionary analysis with Bio3D, *BMC Bioinformatics 15*, 399.

[85] Barman, A., and Hamelberg, D. (2016) Coupled Dynamics and Entropic Contribution to the Allosteric Mechanism of Pin1, *J. Phys. Chem. B 120*, 8405-8415.

[86] Doshi, U., Holliday, M. J., Eisenmesser, E. Z., and Hamelberg, D. (2016) Dynamical network of residue–residue contacts reveals coupled allosteric effects in recognition, catalysis, and mutation, *Proc. Natl. Acad. Sci. U.S.A. 113*, 4735.

[87] Yao, X.-Q., Momin, M., and Hamelberg, D. (2019) Establishing a Framework of Using Residue–Residue Interactions in Protein Difference Network Analysis, *Journal of Chemical Information and Modeling 59*, 3222-3228.

[88] Souffrant, M. G., Yao, X.-Q., Momin, M., and Hamelberg, D. (2020) N-Glycosylation and Gaucher Disease Mutation Allosterically Alter Active-Site Dynamics of Acid-β-Glucosidase, *ACS Catalysis 10*, 1810-1820.

[89] Yao, X.-Q., Momin, M., and Hamelberg, D. (2018) Elucidating Allosteric Communications in Proteins with Difference Contact Network Analysis, *J. Chem. Inf. Model. 58*, 1325-1330.

[90] Allison, R. D., and Purich, D. L. (1979) Practical considerations in the design of initial velocity enzyme rate assays, *Methods Enzymol. 63*, 3-22.

[91] Horecker, B. L., and Kornberg, A. (1948) The extinction coefficients of the reduced band of pyridine nucleotides, *J. Biol. Chem. 175*, 385-390.

[92] Matthews, R. G. (1986) Methylenetetrahydrofolate reductase from pig liver, *Methods Enzymol. 122*, 372-381.

[93] Latovitzki, N., Halper, J. P., and Beychok, S. (1971) Spectrophotometric Titration of Tyrosine Residues in Human Lysozyme, *J. Biol. Chem. 246*, 1457-1460.

[94] Schwans, J. P., Sunden, F., Gonzalez, A., Tsai, Y., and Herschlag, D. (2013) Uncovering the Determinants of a Highly Perturbed Tyrosine pKa in the Active Site of Ketosteroid Isomerase, *Biochemistry 52*, 7840-7855.

[95] Su, D., Aguillon, C., and Gadda, G. (2019) Characterization of conserved active site residues in class I nitronate monooxygenase, *Arch. Biochem. Biophys. 672*, 108058.

[96] Macheroux, P., Massey, V., Thiele, D. J., and Volokita, M. (1991) Expression of spinach glycolate oxidase in *Saccharomyces cerevisiae*: purification and characterization, *Biochemistry 30*, 4612-4619.

[97] Su, D., Yuan, H., and Gadda, G. (2017) A Reversible, Charge-Induced Intramolecular C4a-S-Cysteinyl-Flavin in Choline Oxidase Variant S101C, *Biochemistry 56*, 6677-6690.

[98] Kelly, S. M., Jess, T. J., and Price, N. C. (2005) How to study proteins by circular dichroism, *Biochim. Biophys. Acta 1751*, 119-139.

[99] Leenders, R., Van Hoek, A., Van Iersel, M., Veeger, C., and Visser, A. J. (1993) Flavin dynamics in oxidized Clostridium beijerinckii flavodoxin as assessed by time-resolved polarized fluorescence, *Euro. J. Biochem. 218*, 977-984.

[100] Luo, Y., and Liu, Y.-J. (2016) Bioluminophore and Flavin Mononucleotide Fluorescence Quenching of Bacterial Bioluminescence—A Theoretical Study, *Chem. Eur. J. 22*, 16243-16249.

[101] Sancar, A. (2003) Structure and Function of DNA Photolyase and Cryptochrome Blue-Light Photoreceptors, *Chem. Rev. 103*, 2203-2238.

[102] Su, D., Kabir, M. P., Orozco-Gonzalez, Y., Gozem, S., and Gadda, G. (2019) Fluorescence Properties of Flavin Semiquinone Radicals in Nitronate Monooxygenase, *Chem. Bio. Chem. 20*, 1646-1652.

[103] Weber, G. (1950) Fluorescence of riboflavin and flavin-adenine dinucleotide, *Biochem. J. 47*, 114-121.

[104] Coleman, C. S., Stanley, B. A., and Pegg, A. E. (1993) Effect of mutations at active site residues on the activity of ornithine decarboxylase and its inhibition by active site-directed irreversible inhibitors, *J. Biol. Chem. 268*, 24572-24579.

[105] Rungsrisuriyachai, K., and Gadda, G. (2008) On the Role of Histidine 351 in the Reaction of Alcohol Oxidation Catalyzed by Choline Oxidase, *Biochemistry 47*, 6762-6769.

[106] Rungsrisuriyachai, K., and Gadda, G. (2010) Role of Asparagine 510 in the Relative Timing of Substrate Bond Cleavages in the Reaction Catalyzed by Choline Oxidase, *Biochemistry 49*, 2483-2490

3 THE IONIC ATMOSPHERE EFFECT ON THE ABSORPTION SPECTRUM OF NADH:QUINONE OXIDOREDUCTASE: A REMINDER TO THEORY AND EXPERIMENTALISTS ABOUT THE IMPORTANCE OF SOLUTION IONS

3.1 Abstract

Point charges from ionizable residues in enzymes are commonly utilized to promote substrate binding, catalysis, or protein stability. However, the role of point charges from solution ions in modulating an enzyme's biophysical properties has not been as extensively studied compared to other biomolecules. Previous studies demonstrated solution ions can promote the function of DNA by interacting with the phosphate backbone to stabilize the DNA duplex. A better understanding of the interactions between the charged environment surrounding proteins and protein function is necessary to develop better theories and experiments to elucidate the biophysical properties of proteins. NADH:quinone oxidoreductase (NQO) from *Pseudomonas aeruginosa* PA01 is an FMN-dependent enzyme that contains a tyrosine residue (Y277) in the active site distanced 3.0 Å from the C_7 methyl group of the flavin. In the study, the UV-visible absorption spectrum of NQO was investigated and compared to that of the mutant enzyme NQO-Y277F, which determined Y277 deprotonates to a tyrosinate at high pH without affecting the absorption spectrum of the flavin cofactor. QM/MM simulations of NQO with Y277 in the neutral and anionic forms predicted that introducing a negative charge near the C_7 methyl group of the flavin impacts flavin's absorption properties. In contrast, QM/MM simulations indicated deprotonating Y277 has no effect on flavin's absorption spectrum when solution ions were included in the simulations, which is consistent with the biochemical experiment. An "average solvent electrostatic configuration" QM/MM method was utilized to demonstrate the solution ions mask the effect of deprotonated Y277 by arranging themselves around the protein-solvent interface

to form an “ionic atmosphere”. As a result, the UV-visible absorption spectra of NQO were determined in the presence and absence of NaCl which revealed deprotonated Y277 decreases the flavin’s absorption intensity at the 461 nm peak and redshifts both peaks. The results presented here demonstrate an unexpected long-distance interaction between solvent ions and the active site of NQO that serves to prevent the flavin’s absorption spectrum from being altered by deprotonated Y277.

3.2 Introduction

Ions are well known to play a critical role in biology by modulating the function of lipids[1-3], nucleic acids[4-7], and proteins[8-11]. For instance, ionizable residues in the active site of enzymes can promote substrate binding or catalysis, as demonstrated in xylanase[11], glucose oxidase[8, 12], ketosteroid isomerase[13], and UDP-galactose 4-epimerase.[14] In contrast, ionizable amino acids on protein surfaces can stabilize protein structures as previous studies demonstrated optimizing residue-residue charge interactions at the protein's surface leads to an increase in thermodynamic denaturation temperatures and denaturation Gibbs free energies.[15-17] Ions also promote the stability of DNA, where the alkaline metal cations Na^+ and K^+ localize at the major and minor grooves of the phosphate backbone to stabilize the DNA duplex and allow for proper functionality.[7, 18, 19] The local positions of the monoatomic ions varies with the sequence motifs of DNA, suggesting that several sequence-dependent properties of the DNA duplex can be attributed to the localization of cations.[20] Monoatomic solution ions play a role in protein chemistry by modulating protein solubility and stability[21-23]; however, the relationship between solution ions, protein surface charges, and active site ionizable residues is not as well understood in proteins as it is in DNA. There exists a need to understand better the interactions between solution ions and the point

charges in protein chemistry to develop better theories and experiments that fully consider the proteins' environment.

UV-visible absorption spectroscopy is an important tool commonly used to probe the environment surrounding aromatic amino acid residues and conjugated cofactors in proteins. A recent investigation on the ionizable active site residues found in class I nitronate monooxygenases (NMOs) utilized UV-visible absorption spectroscopy to demonstrate a tyrosine deprotonates at high pH to form a negative point charge in the active site of the flavin-dependent NMO from *P. aeruginosa* PA01 (PaNMO).[24] However, PaNMO contains four active site tyrosines, and the study was unable to establish which tyrosine deprotonated to a tyrosinate. Currently, no known flavoprotein has been utilized to identify a deprotonating active site tyrosine and probe the effect of a tyrosinate on the absorption spectrum of flavin. Investigating the relationship between an active site tyrosinate and the UV-visible absorption spectrum of flavin would help build on our understanding of how perturbations in flavin absorption peaks probe the active site environment of flavoproteins.

Flavin is an organic, conjugated cofactor responsible for a wide variety of one- and two-electron oxidations and reductions. The flavin cofactor is a multi-redox molecule and can be found in the quinone, semiquinone, or hydroquinone redox states (**Fig. 3.1A**).[25] Redox states can be distinguished by studying the UV-visible absorption spectrum of flavins because each redox state absorbs light at distinct excitation peaks (**Fig. 3.1B**).[26] Flavin is also capable of sampling multiple protonation states due to the isoalloxazine ring moiety, which contains an ionizable nitrogen group (N_3) with a pK_a of 10.3.[27-29] The various redox and protonation states of flavin allow biochemists to utilize flavin's UV-visible absorption spectrum to probe catalysis, substrate binding, and the active site microenvironment in flavoenzymes.[28] Previous studies have utilized oxidized flavin to

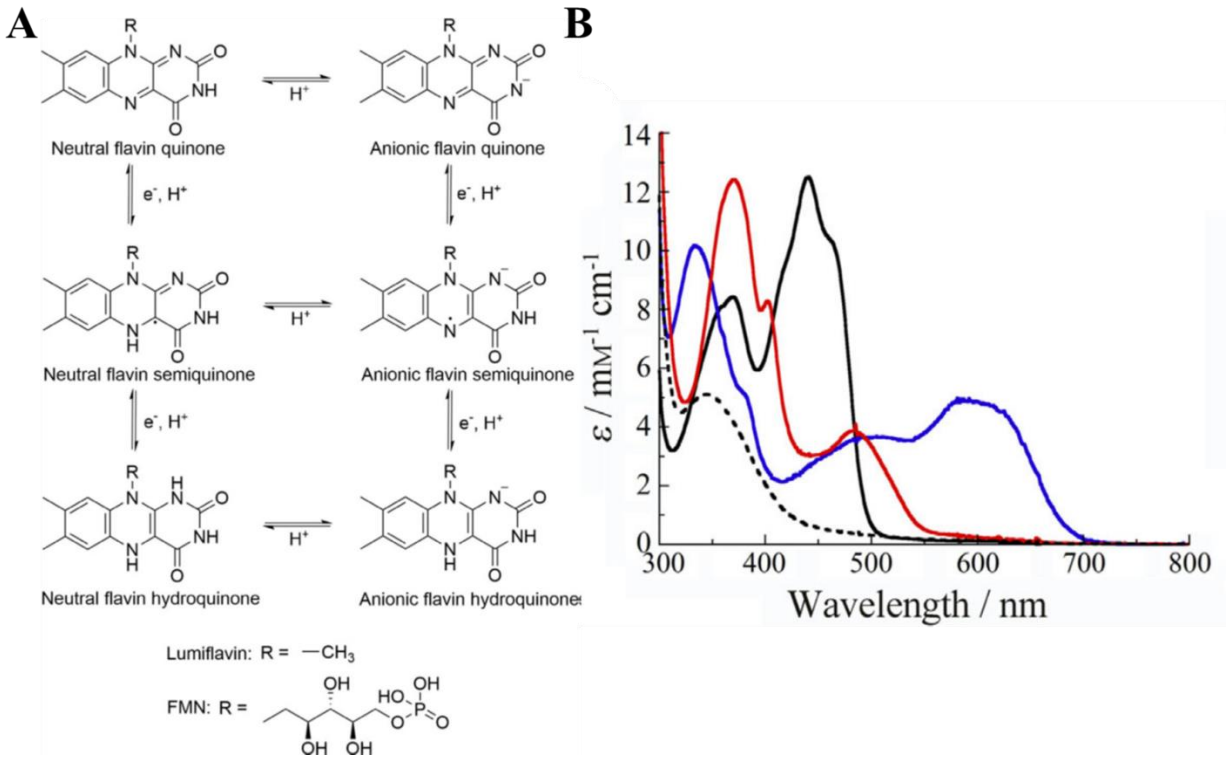

Figure 3.1. Redox States of Flavin.
(A) The structure of flavin in the various redox states is shown. (B) The UV-visible absorption spectra for PaNMO are shown where the flavin cofactor is in the oxidized (black, solid line), neutral semiquinone (blue), anionic semiquinone (red), and hydroquinone (black, dashed line) redox states. The oxidized spectrum was recorded in 20 mM piperazine, pH 10.0, 0.1 M sodium chloride, while semiquinone spectra were recorded in the same buffer with 20% glycerol at pH 5.0 (neutral) and 10.0 (anionic). The hydroquinone spectrum was recorded in 200 mM piperazine, pH 10.0, after an anaerobic reduction with 5 mg sodium borohydride. Adapted with permission from D. Su et al., Fluorescence properties of flavin semiquinone radicals in nitronate monooxygenase, Chem. Bio. Chem. 20, 13 (2019) 1646-1652

demonstrate the flavin's absorption spectrum varies in the presence of negatively charged substrates and solvents (**Fig. 3.2 top**).[26, 30, 31] However, a better understanding of the relaionship between charged amino acid side chains in the active site of flavoproteins and flavin's absorption spectrum is required to fully utilize flavins as a spectroscopic probe of its environment.

Electrostatic spectral tuning maps (ESTMs) are an intuitive computational tool used to understand how localized charges in a chromophore's vicinity affect that chromophore's absorption wavelength and intensity.[25, 32] Tuning maps for the 460 nm peak (E_1 and f_1) and the 360 nm peak (E_2 and f_2) of oxidized flavin are presented here to indicate how a negative, localized

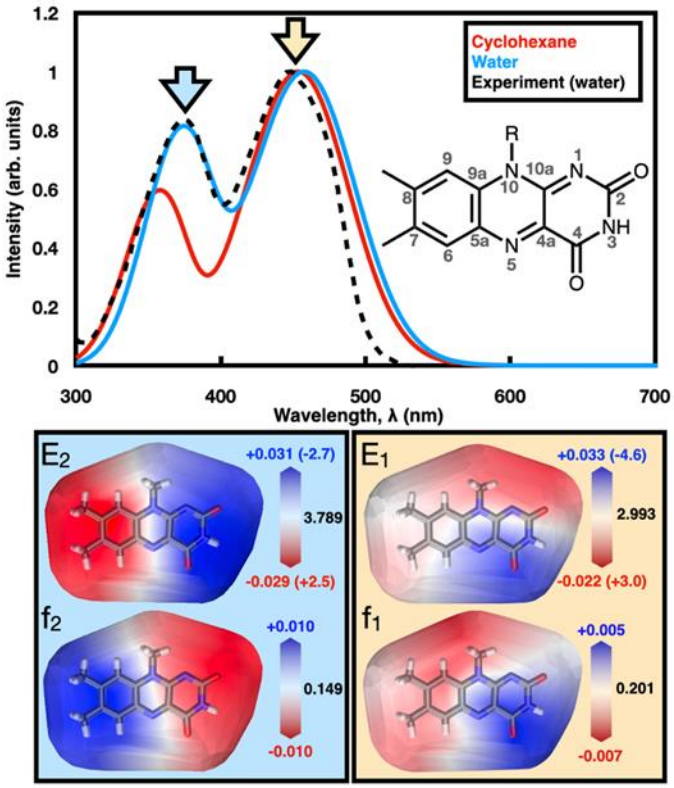

Figure 3.2. Effect of the Surrounding Environment on Flavin Absorption Peaks.
Top: *Simulated UV-visible absorption spectrum of flavin in a polar (water) and non-polar (cyclohexane) solvent. The experimental UV-visible absorption spectrum in water is also shown* [26] *Flavin has two near-UV-visible absorption bands, labeled band 1 (yellow arrow) and band 2 (blue arrow). The inset shows the structure of flavin with atom labels. Adapted from ref. 25.* ***Bottom****: Electrostatic spectral tuning maps (from ref. 32) and oscillator strength tuning maps (this work) showing how negative 0.1e charges placed on flavin's van der Waals surface affect the absorption wavelength (E_1 and E_2) and oscillator strength (f_1 and f_2) for each of its two absorption bands 1 and 2, respectively. The E_1/E_2 map legends indicate the magnitude of the shifts relative to the gas-phase reference excitation energy in eV (nm in parentheses) caused by the -0.1e charge, while the f_1/f_2 map legends indicate the change in the oscillator strength relative to the gas-phase reference strength. The approach to compute such maps is described in ref. 32, using the B3LYP/6-31+G* method and basis set.*

charge at each position of the flavin's van der Waals surface affects flavin's absorption spectrum (**Fig. 3.2 bottom)**. For instance, the ESTMs demonstrate that negative charges near flavin's C_7 methyl group would result in a noticeable redshift (E_2) and increase in oscillator strength (f_1, related to absorption intensity) at the 360 nm peak. In contrast, negative charges near the flavin's C_7 methyl group would result in either no shift or a weak redshift (E_1) and a slight decrease in oscillator strength (f_1) at the 460 nm peak. The absorption spectra and ESTMs with flavin presented here demonstrate the relative absorption intensities of the flavin's peaks are much more sensitive

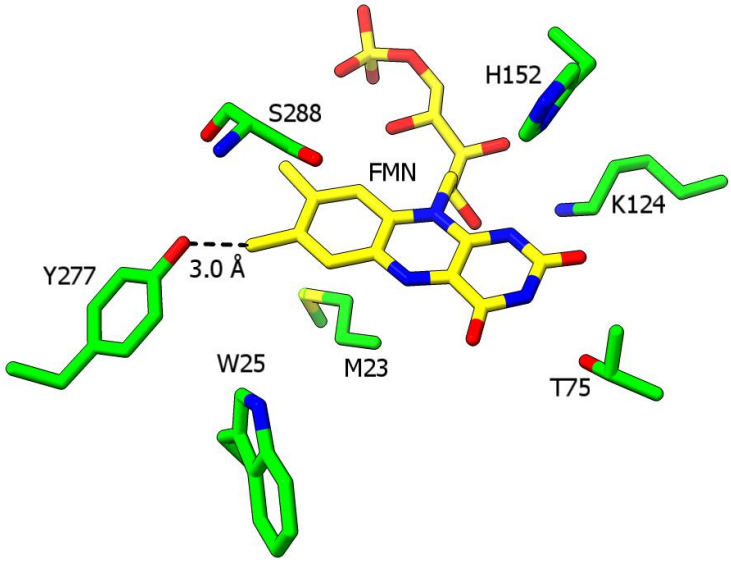

Figure 3.3. The Active Site of NQO.
The active site of NQO depicting the positions of the FMN cofactor and key active site residues (PDB: 2JGL). A 3.0 Å distance from the hydroxyl O atom of Y277 to the C atom on the C_7 methyl group of FMN was determined. The carbon atoms for FMN are shown in yellow while the carbon atoms of the protein are shown in green. Nitrogen and oxygen atoms are colored in blue and red, respectively.

to the surrounding electrostatic environment than the peak wavelengths. For example, the computed absorption spectra of flavin in different solvents with varying polarity demonstrates the 360 nm peak's absorption intensity is ~30-40% brighter in water than in cyclohexane **(Fig 3.2 top**).[25] A central hypothesis in this work is that we can use flavin's peak intensities to probe local and long-range electrostatics in a flavoprotein.

NADH:quinone oxidoreductase (NQO, E.C. 1.6.5.9, UniProtKB Q9I4V0) from *P. aeruginosa* PA01 is an FMN-dependent enzyme that utilizes NADH to catalyze a two-electron reduction of quinones.[33] Quinone reductases (QR) are flavin-dependent enzymes that detoxify quinones to form hydroquinones and bypass the production of the highly reactive semiquinone radical species.[34, 35] QRs play an antioxidant protective role in the cell by preventing semiquinone radicals from reacting with molecular oxygen to promote oxidative stress, which results in tissue degeneration, apoptosis, premature aging of cells, and neoplasia.[36, 37] Oxidative stress is a process

found in both prokaryotes and eukaryotes; thus, QRs have been reported to protect against quinone-related cell damage in a wide variety of organisms such as bacteria[38, 39], fungi[40, 41], plants[42, 43], and mammals.[44, 45] A crystal structure of NQO in the ligand-free form revealed the enzyme's active site contains several ionizable groups, including K124, H152, S288, and Y277.[46] Y277 is especially of interest as its hydroxyl group is 3.0 Å away from the C_7 methyl group of the flavin's isoalloxazine ring (**Fig. 3.3**). Besides the close proximity to the flavin, Y277 is mostly exposed to the active site's bulk solvent. Investigating the position of Y277 in the active site of NQO suggests the residue may be used to elucidate further the relationship between the flavin's electrostatic environment and its absorption spectra.

In this study, Y277 in NQO was replaced with a phenylalanine to probe the differences in tyrosine deprotonation between the mutant and wild-type enzymes, which determined Y277 deprotonates to a tyrosinate at high pH. NQO-WT at high pH was investigated through a combination of biochemical and computational techniques to assess the effect of the unprotonated Y277 near the flavin's C_7 methyl group on the flavin's absorption spectrum. ESTMs presented above suggest that forming a negative charge by deprotonating Y277 will increase the absorption intensity and redshift the 360 nm peak while slightly decreasing the absorption intensity of the 460 nm peak (**Fig. 3.2**). However, the UV-visible absorption spectra and hybrid quantum mechanical/molecular mechanical (QM/MM) calculations presented in this study indicate that solution ions surrounding the protein form a long-range electrostatic interaction to counter the effect of deprotonated tyrosinate on flavin's absorption spectrum.

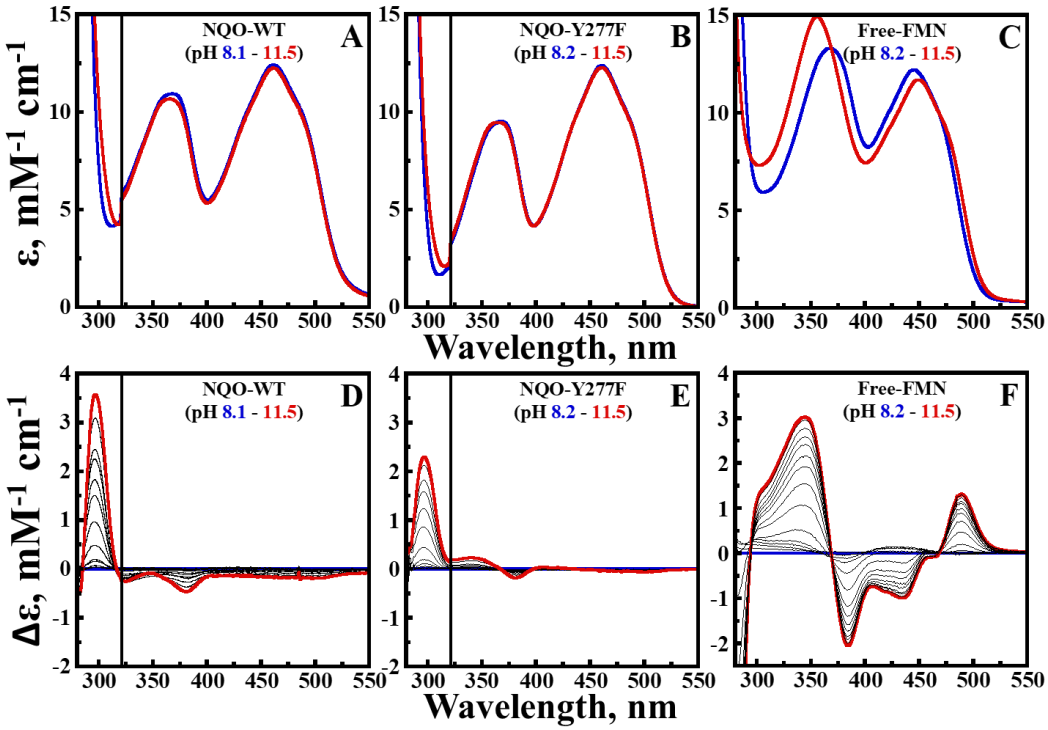

Figure 3.4. Effect of pH on the Absorption Spectra of NQO-WT, NQO-Y277F, and Free-FMN.

Absorption spectra for (A) NQO-WT, (B) NQO-Y277F, and (C) free-FMN are shown as pH increases from 8.0 (blue) to 11.5 (red). Difference absorption spectra for (D) NQO-WT, (E) NQO-Y277F, and (F) free-FMN are shown where the spectra at pH 8.0 was used as a baseline. Extinction coefficient values for the enzyme systems were corrected for the protein absorption (≥320 nm) by adjusting for flavin binding. The FMN/enzyme stoichiometry is 0.8 for NQO-WT and 0.7 for NQO-Y227F.

3.3 Results and Discussion

3.3.1 Deprotonation of Y277 in NQO

The protonation state of Y277 was investigated by probing the effect of pH on the UV-visible absorption spectra of NQO-WT and comparing the results to those of NQO-Y277F. Absorption spectra were taken incrementally as the pH was adjusted from 8.0 to 11.5. Spectral changes at 295 nm were monitored as a function of pH to assess the protonation state of all tyrosine residues throughout both enzymes, where NQO-WT contains four tyrosine residues (**Fig. 3.4AB**).[13, 24, 47] For NQO-WT and NQO-Y277F, the most significant spectral changes were found at 295 nm with maximal increases of 3.5 and 2.3 $mM^{-1}cm^{-1}$, respectively (**Fig. 3.4DE**). The 1.2

$mM^{-1}cm^{-1}$ decrease in the $\Delta\varepsilon_{295}$ value from NQO-WT to NQO-Y277F suggests the Y277F mutation altered the deprotonation of tyrosine residues in NQO. Structurally, NQO-Y277F differs from the wild-type enzyme by the removal of the hydroxyl O atom of Y277, suggesting that any changes in the absorption spectra of NQO by this mutation are likely due to the absence of the hydroxyl group. Thus, comparing the absorption spectra of both enzymes probes the protonation state of Y277, where the additional tyrosine deprotonation event that occurs in NQO-WT indicates that Y277 deprotonates at high pH. There is a possibility that removing the hydroxyl group of Y277 altered the environment and thus the deprotonation of the three other tyrosine residues in NQO; however, this is less likely as the hydroxyl group of Y277 is about 15 Å from the hydroxyl groups of the other tyrosines. The $\Delta\varepsilon_{295}$ values were plotted versus pH for both enzymes using Eq 1. to determine the pK_a values corresponding to the tyrosine residues' ionization in each enzyme system (**Fig. 3.5A**). A pK_a value of 11.1 ± 0.1 was determined for Y277 by taking the difference in $\Delta\varepsilon_{295}$ values between NQO-WT and NQO-Y277F (**Fig. 3.5B**). The results indicate that the

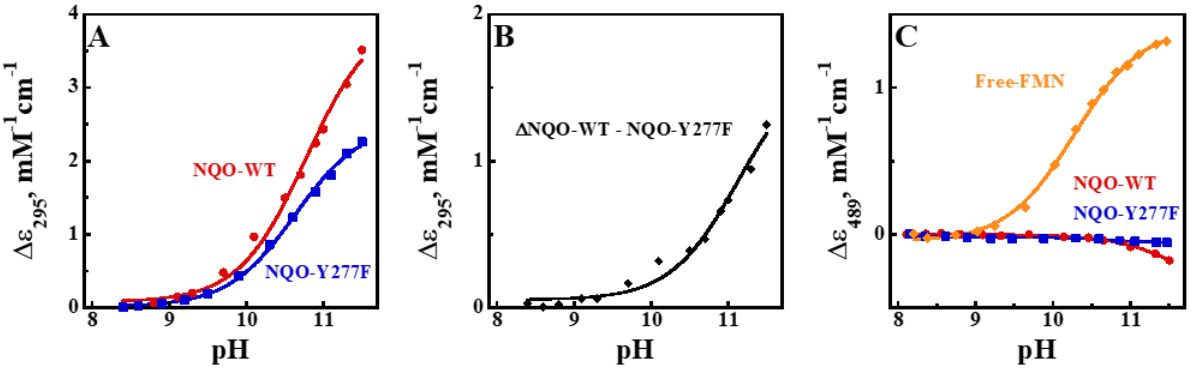

Figure 3.5. Ionization of Active Site Residues in NQO-WT, NQO-Y277F, and free-FMN.
(A) A plot of the Δε values at 295 nm as a function of pH is shown for NQO-WT and NQO-Y277F. (B) The difference in the Δε values at 295 nm between the two enzymes was determined. Data points are from the 295 nm peak of the difference absorption spectra for NQO-WT and NQO-Y277F taken as a function of pH. (C) A plot of the Δε values at 489 nm as a function of pH is shown for all systems. Data points are from the 489 nm peak of the difference absorption spectra for each system taken as a function of pH. Curves were fit to datapoints using Eq. 1.

hydroxyl side chain of Y277 is neutral at pH 8.0 and anionic in ~60% of the wild-type enzyme population at pH 11.5.

The absorption spectra of free FMN in solution (free-FMN) were assessed and compared to those of NQO-WT to determine if the protonation state of the N_3 atom was altered in NQO as pH increased from 8.0 to 11.5 (**Fig. 3.4C**). Although the ionization of the flavin's N_3 atom is well-established[27-29, 48-50], the authors were unable to find a figure depicting the titration of free-FMN in the literature. The difference peaks correlating to N_3 deprotonation in free-FMN were observed at 340, 380, 435, and 490 nm (**Fig. 3.4F**). A pK_a value of 10.2 ± 0.1 was measured for free-FMN by plotting the $\Delta\varepsilon_{489}$ values versus pH, which agrees with previous studies that investigated the ionization of the flavin's N_3 atom in bulk solvent (**Fig. 3.5C**).[27-29] The absorption spectra for neither NQO-WT nor NQO-Y277F depicted the difference peaks characteristic of N_3 deprotonation, suggesting that deprotonating the hydroxyl side chain of Y277 does not affect the ionization of the flavin cofactor in the active site of NQO at the pH range observed for the flavin in bulk solvent.

3.3.2 Effect of the Y277F Mutation on the Steady-State Kinetics of NQO.

The steady-state kinetic parameters of NQO-Y277F were investigated and compared to those of NQO-WT to determine if the Y277F mutation perturbed the turnover, and therefore the active site structure of NQO (**Table 3.1**). Initial rates of reaction were determined by varying the concentrations of both NADH and benzoquinone at pH 7.0. Steady-state kinetic parameters were assessed by fitting the kinetic data to an equation describing a ping-pong bi-bi steady-state kinetic mechanism (Eq. 2) where the fits with the highest R^2 value were chosen. Comparing NQO-Y277F to NQO-WT illustrated a < 3.0-fold change in all the measured kinetic parameters (**Table 3.1**). The K_{NADH} value was not determined for NQO-WT as the lowest concentration of NADH tested

was above 50% saturation. The results indicate only modest changes in the steady-state kinetic parameters due to the Y277F mutation, suggesting the mutation had a negligible impact on the organization of key catalytic residues and structure in NQO at pH 7.0. The kinetic comparison between enzymes also indicates Y277 has a negligible role in substrate capture, catalysis, and product release in NQO since large changes in k_{cat} and K_{BQ} values would be expected if Y277 did play a mechanistic role.

Table 3.1. Steady-State Kinetic Parameters of NQO-WT and NQO-Y277F at pH 7.0.

Kinetic Parameter	NQO-WT	NQO-Y277F
k_{cat}, s^{-1}	33 ± 2	42 ± 3
K_{BQ}, μM	21 ± 3	55 ± 6
K_{NADH}, μM	ND[a]	54 ± 7
k_{cat}/K_{BQ}, $M^{-1}s^{-1}$	1,600,000 ± 300,000	800,000 ± 100,000
k_{cat}/K_{NADH}, $M^{-1}s^{-1}$	ND[a]	800,000 ± 100,000
R^2	0.979	0.994

Kinetic parameters were determined with varying concentrations of NADH and benzoquinone in 20 mM KP_i, pH 7.0, and 100 mM NaCl at 25 °C.
[a]Values were not determined because concentrations of NADH below 50% saturation with NQO-WT could not be tested.

3.3.3 Effect of Deprotonating Y277 on the UV-visible Absorption Spectra of FMN in NQO.

The UV-visible absorption spectrum of NQO was measured from pH 8.0 to 11.5 to determine the effect of deprotonating Y277 on the flavin cofactor's absorption peaks **(Fig. 3.4AD)**. Although Y277 deprotonation effectively introduces a negative charge near the C_7 methyl group of the flavin, the absorption wavelengths and intensities of the 368 and 461 nm peaks of oxidized NQO remained unaffected (**Fig. 3.4A**). The lack of an effect is surprising considering the tuning maps presented in Fig. 3.2 indicated that at least the wavelength and the intensity of flavin's 368 nm peak should be sensitive to a negative charge introduced at residue 277.[25] Y277 is mostly

exposed to the bulk solvent in the active site of NQO; furthermore, there are no other ionizable residues in the active site that could potentially act as counterions to cancel out the effect of the tyrosinate. To better understand the effect of deprotonating Y277 on the absorption spectrum of FMN, QM/MM simulations were performed on NQO in solution.

3.3.4 MD and Hybrid QM/MM Simulations and Computations

Molecular dynamic (MD) and Hybrid QM/MM simulations were performed on NQO-WT with both protonated and unprotonated Y277 to investigate the lack of an effect by Y277 deprotonation on the flavin's spectroscopic properties in solution. MD simulations indicated that the side chain of Y277 in both the protonated and unprotonated forms occupied the same space in the active site of NQO due to a hydrogen bond with the backbone nitrogen atom at residue 288.[51]

The average solvent electrostatic configuration–free energy gradient (ASEC-FEG) method was used for the QM/MM calculations, as described below (**Section 3.5.8**). The ionization states of amino acids other than Y277 were determined with PROPKA. When Y277 is protonated, the

Table 3.2. QM/MM Computed Oscillator Strengths and Excitation Wavelengths for Flavin Peaks in NQO.

Y277 Ionization State	n_{Cl-}	n_{Na+}	f_1	f_2	E_1, nm	E_2, nm
Neutral	2	0	0.087	0.270	428	361
Anionic	1	0	0.057 (-30%)	0.322 (+19%)	434 (+6 nm)	369 (+8 nm)
Neutral	20	18	0.142	0.187	417	340
Anionic	19	18	0.145 (+2%)	0.183 (-2%)	418 (+1 nm)	339 (-1 nm)
Anionic (deleted ions)	1	0	0.134 (-6%)	0.210 (+12%)	421 (+4 nm)	345 (+5 nm)

QM /MM (TD-B3LYP/aug-cc-pVDZ/AMBER) computed oscillator strengths (f_1 and f_2) and excitation wavelengths (E_1 and E_2) for flavin's first and second absorption peaks are shown, respectively. The numbers in parentheses indicate the % change in oscillator strength and the absolute change in excitation wavelength in nm upon deprotonation of Y277 for that model. The last row shows the results for the same QM/MM structure as the previous row but in the absence of 18 Na^+ and Cl^- ions from the QM/MM calculation

protein had a total charge of +2 due to the number of positively charged amino acids outnumbering the number of negatively charged amino acids in the protein. Therefore, as often done in the construction of protein QM/MM models, the system was neutralized using two chloride ions (n_{Cl^-} = 2). In the model with a unprotonated Y277, the total charge of the protein was +1, where one Cl^- is used to neutralize the system (n_{Cl^-} = 1). The spectral properties computed using the QM/MM models indicated that deprotonating Y277 would lead to a ~7 nm redshift at both peaks, a 19% increase in intensity at the 368 nm peak, and a 30% decrease in intensity at the 461 nm peak (top two rows in **Table 3.2**). The results presented here are consistent with the tuning maps in Fig. 3.2; however, the QM/MM calculations do not explain the lack of changes in the flavin's absorption peaks in NQO when Y277 deprotonates in solution.

It is important to note that the spectra obtained in Fig. 3.4 were not for NQO in a pure water solvent, but rather the enzyme was in a buffered solution of 10 mM NaP_i, 10 mM NaP_iP_i, 100 mM NaCl, and 20% glycerol. To better understand the effect of solution ions on the absorption spectra of flavin, the QM/MM simulations were repeated in the presence of Na^+ and Cl^- ions. QM/MM simulations mimicked the concentration of 100 mM NaCl from the biochemical experiment by adding 18 Na^+ and Cl^- ions to the system, where extra Cl^- ions were added to neutralize the protein charges. QM/MM models tend to place ions into specific positions; thus, ASEC-FEG was employed to sample the solution ions' positions properly. Utilizing ASEC-FEG for QM/MM calculations means that the solution ions were each replaced by 100 pseudo-ions, with a charge of ±0.01*e*, where their positions were sampled by MD.[52-58] Thus, simulating 18 Na^+ ions translates to 1800 +0.01*e* point charges where the positions originate from 100 MD snapshots. Comparing the QM/MM calculations for Y277 in the neutral and anionic forms in the presence of solution ions yielded a ≤ 2% change in the computed flavin peak's intensities and a ≤ 1 nm shift in peak

wavelengths (rows 3 and 4 in **Table 3.2**). The results of the QM/MM calculations in the presence of solution ions agree with the biochemical experiment in Fig. 3.4 by demonstrating that solution ions appear to cancel out the effect of deprotonating Y277 on the flavin's absorption spectrum. To confirm the addition of salt ions did, in fact, mask the effect of the unprotonated Y277 on flavin's absorption spectrum, calculations with the QM/MM APEC configuration containing 18 NaCl pairs were re-run, where the added salt ions were deleted, leaving only the equivalent of 2 Cl^- ions (see the last row of **Table 3.2**). Following the removal of the solution ions from the simulation space, perturbations in the absorption peaks of flavin were observed that were consistent with the tuning maps, which predicted the effect of a negatively charge tyrosinate near the flavin's C_7 methyl group in NQO. The results presented here indicate that the solution ions mask the effect of deprotonating Y277 on flavin's absorption spectrum, where the effect can be investigated once the solution ions are removed from the system.

3.3.5 Radial Distribution Functions

To better understand how Na^+ and Cl^- ions modulate the UV-visible absorption spectrum of flavin, the radial distribution functions (RDFs) of the Na^+ and Cl^- ions relative to the flavin's center of mass were computed from a 500 ns MD simulation. Additionally, the coordination numbers (CNs) were calculated, which describes the spherical integral of the RDF at each radial position from the flavin. RDF calculations with solutions ions and Y277 in the neutral and anionic forms were performed, where the difference in the RDF and CN values between Na^+ and Cl^- ions were calculated (black lines **Fig. 3.6**). For comparison, the RDF calculations were performed with the NQO simulations that did not contain added NaCl but instead only included Cl^- ions to keep the system globally neutral (green lines **Fig. 3.6**). Comparing the ionic environment of NQO with Y277 in the neutral and anionic forms demonstrated that the distribution of the solution ions

surrounding the protein is altered upon Y277 deprotonation. It is important to note that the model with Y277 in the anionic form contained one less Cl^- ion than the model with Y277 in the neutral form; however, the resulting +1 overall charge was not distributed equally between each radial shell surrounding the flavin. The displacement of the solution ions is reminiscent of the "ionic atmosphere" effect described in the Debye–Hückel theory,[59] where each charge is surrounded, on average, by a "cloud" of oppositely charged ions.

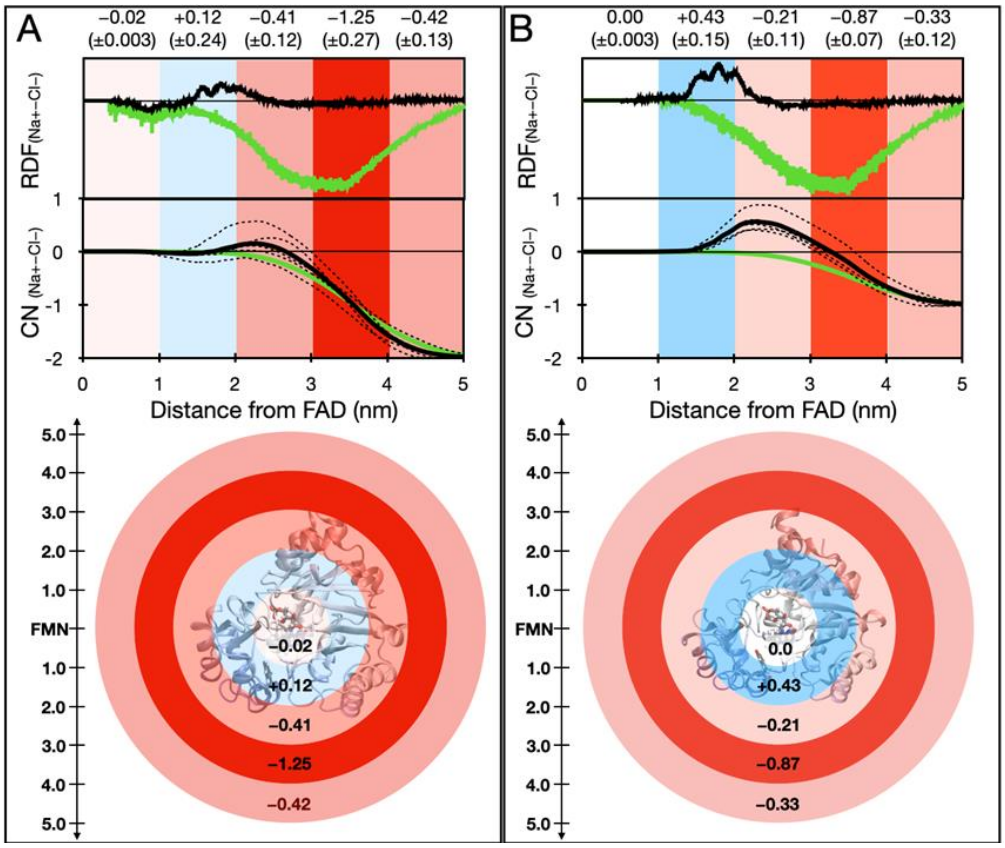

Figure 3.6. Distribution of Solution Ions in NQO QM/MM Simulations.
Top*: RDFs of solution ion charges (computed as the difference between the RDFs of the Na^+ and Cl^- ions) for a 500 ns MD simulation of NQO with a (A) neutral and (B) anionic Y277 and including 18 added Na^+ and Cl^- ions to mimic a 100 mM NaCl solution. Below the RDF is a plot of the corresponding CN as a function of distance for the full 500 ns trajectory (bold line) and for 100 ns windows (thin dashed lines). The numbers at the top indicate the total change in CN (i.e., integral of the RDF) for five different shells around flavin, each 1 nm thick. The associated plus/minus uncertainty is the standard deviation calculated by averaging the result from five 100 ns windows (dashed lines).* ***Bottom****: The results of the integrated RDFs for each shell up to 5 nm (i.e., the change in CN for that shell) plotted on top of the protein structure (close to actual scale). This plot helps visualize where solution ion density changes occur relative the protein.*

To ensure the results presented here are not due to a statistical anomaly, the CN calculations for the full 500 ns trajectory (bold lines in **Fig. 3.6**) were compared with the CN calculations during each 100 ns window within the 500 ns production (thin dashed lines). The comparison between the 500 ns and 100 ns windows consistently showed an increase in the density of Na^+ ions near the protein surface from the protonated to deprotonated Y277 models; however, the ion distribution was not fully consistent between the 100 ns windows. The fluctuations between the 100 ns windows indicate that substantially longer molecular dynamics may be needed to capture consistent ion distributions.

Following Y277 deprotonation, Na^+ ions do not enter the active site pocket in NQO to mask the effect of anionic Y277 on the flavin's absorption spectrum. Instead, the deprotonation of Y277 leads to an increase in the positive charge density 1-3 nm away from the flavin, indicating that Na^+ ions move closer to the protein surface and/or the Cl^- ions move away from the protein surface once the hydroxyl O atom of Y277 forms a negative charge. Evidence to support these conclusions comes from the RDF calculations with NQO, where Y277 was modeled in the neutral and anionic forms. Once Y277 deprotonated in the active site of NQO, a slight increase of 0.02 in the positive charge density was seen $\leq$ 1 nm away from the flavin. In contrast, increases $\geq$ 0.10 in the positive charge density 1-3 nm away from the flavin were observed in NQO from neutral to anionic Y277. The redistribution of ions is most likely responsible for canceling out the effect of the localized negative charge from Y277 on the flavin's absorption spectrum and therefore acts as a long-range electrostatic spectral tuning mechanism. Interestingly, the redistribution of solution ions was entirely missed in the models containing only Cl^- ions to keep the simulations globally neutral. The results presented here demonstrate the need to consider the effect of solution ions in

QM/MM models as computational models that do not contain added solution ions will incorrectly predict that deprotonating Y277 will have a strong effect on flavin's absorption spectra.

3.3.6 Effect of Added Ions on the UV-Visible Absorption Spectra of NQO

The UV-visible absorption spectra of NQO in the presence and absence of NaCl were measured in solution to investigate whether NaCl ions can indeed have a long-range electrostatic effect on flavin's absorption spectrum. Absorption spectra were first determined in 10 mM piperidine, where drops of NaOH were discretely added to buffer the solution at pH 11.5 and minimize the solution's concentration of counterions. After taking a spectrum of NQO with minimal counter ions, 100 mM NaCl was added to the solution, which increased the solution's ionic strength from 10 to 110 mM. The absorption spectra of flavin displayed a 19% increase at the 461 nm peak, a 41% increase at the 368 nm peak, and an 8 nm blueshift at both peaks by the addition of NaCl (**Fig. 3.7A**). Isosbestic points formed at 291 and 480 nm suggesting the enzyme did not denature following the addition of NaCl. QM/MM calculations on NQO investigated the

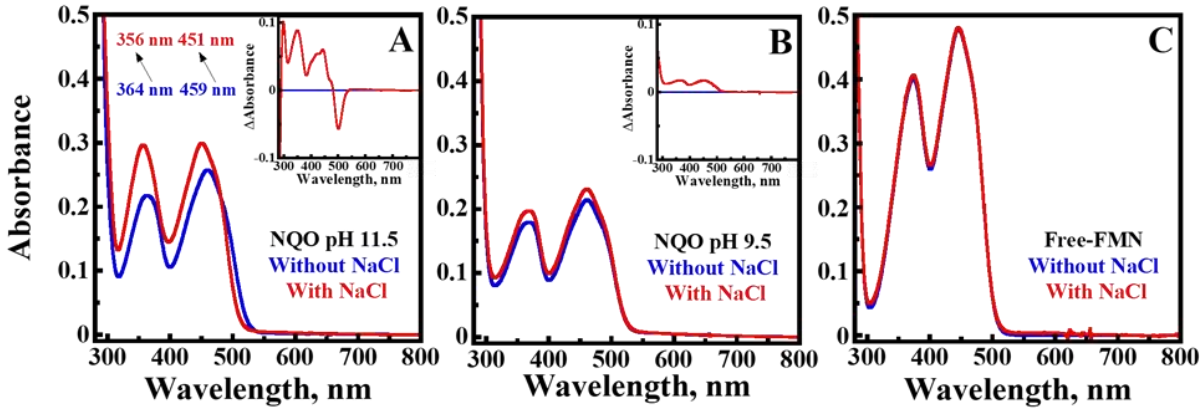

Figure 3.7. Absorption Spectra of NQO and Free-FMN With and Without NaCl.
UV-visible absorption spectra of (A) NQO at pH 11.5, (B) NQO at pH 9.5 and (C) free-FMN at pH 8.0 in the absence of NaCl (blue) and presence of 100 mM NaCl (red) is shown. Enzyme spectra were recorded in 50 mM piperidine, while free-FMN was recorded in 10 mM HEPES at 10 °C. Spectra were recorded 2 min after the addition of NaCl, apart from NQO at pH 11.5 which took an hour to equilibrate. The inserts in panel A and B show the difference in the absorption spectra following the addition of NaCl. Spectra are reported in absorbance instead of extinction coefficient values as extinction coefficient values for all systems were previously reported in the presence of salt.

absorption spectrum of flavin following Y277 deprotonation (**Table 3.2**), whereas the experiment presented here probes the effect of masking the interactions between unprotonated Y277 and flavin's absorption spectra by the addition of solution ions (**Fig. 3.7A**); thus, we expect the changes in the flavin's absorption spectra presented here to be qualitatively opposite to that of the computational calculations. Indeed, the increase in intensity at the 461 nm peak and blueshifts of both flavin peaks seen in Fig 3.7A are consistent with the QM/MM calculations, suggesting the effect of unprotonated Y277 on flavin's absorption spectrum can be elucidated biochemically when the absorption spectra of NQO is investigated in a solution mostly absent of solution ions.

The absorption spectra of NQO-WT at pH 9.5 and free-FMN at pH 8.0 with and without NaCl were investigated to confirm the spectral changes in NQO-WT at pH 11.5 were due to the solutions ions masking the effect between unprotonated Y277 and the flavin cofactor. Following the addition of 100 mM NaCl to NQO-WT at pH 9.5, there were no shifts in wavelength and a < 10% increase in intensity at both absorption peaks of flavin (**Fig. 3.7B**). In comparison, there were no changes in peak intensity or wavelength at both absorption peaks for free-FMN following the addition of NaCl (**Fig. 3.7C**). The absorption spectra for free-FMN were recorded at pH 8.0 as the previously reported pK_a value for the N_3 atom suggests the flavin would not be fully oxidized at higher pH values (**Fig. 3.4F**). The results demonstrate NQO at pH 11.5 was the only system to observe spectral changes by the addition of NaCl, which is consistent with the solution ions masking the effect of a negative charge near the flavin's C_7 methyl group.

3.4 Conclusion

Solution ions are well known to play an essential role in protein chemistry by stabilizing conformations, assisting in protein folding, and altering enzymatic reaction rates.[21-23,60-62] However, the electronic contributions of solution ions to biomolecular systems are not entirely

understood; thus, there remains an ongoing effort to model the electrostatics of ionic solutions for applications in academia, medicine, and engineering fields. [49,63-66] A model describing electrostatic interactions at the protein-solvent interface suggests that while short-distance interactions are reasonably accurate, long-distance interactions have not been fully elucidated and maintain some inaccuracies.[21] Here, we describe an unexpected long-distance interaction between solution ions and the absorption spectrum of flavin in NQO.

In this joint computational and biochemical study, NQO is utilized to demonstrate the active site tyrosine Y277 deprotonates at high pH to introduce a negative charge 3.0 Å from the C_7 methyl group of the flavin cofactor. Initial biochemical and computational techniques were employed using protocols considered standard in their respective fields to determine how unprotonated Y277 would alter the absorption spectrum of flavin. Multiple computational models consistently predict that deprotonating Y277 would impact flavin's absorption peak intensities and wavelengths; however, no changes in the UV-visible absorption spectrum of NQO are observed when Y277 deprotonates. The main disparity between the two experiments was determined to be the presence of solution ions, where the absorption spectrum of NQO was taken in the presence of 100 mM NaCl, while the QM/MM simulations contained only a few Cl^- ions to keep the system globally neutral. Interestingly, when the QM/MM computations were carried out in the presence of added solution ions, the results were consistent with the biochemical study, which determined no effect. In comparison, when the UV-visible absorption spectrum of NQO was investigated in a solvent mostly absent of solution ions, spectral perturbations predicted by the initial QM/MM calculation were observed. Additionally, the radial distribution function of the solution ions from the QM/MM simulations indicated that the solution ions rearrange to generate a more positive charge density near the protein surface when Y277 deprotonates, which generates a long-range

counterion effect to the active site tyrosinate through an “ionic atmosphere”. Solution ions can affect biomolecules in many ways, some of which are not fully understood by the scientific community. The results suggest a unique and unexpected counterion interaction forms between NQO and the solution ions to prevent unprotonated Y277 from altering flavin’s absorption spectrum. The current study should serve as an important reminder to biochemical and computational chemists not to overlook the contributions of solution ions to proteins' biophysical properties when developing experiments and theories.

The current study suggests that deprotonating Y277 modulates the absorption spectrum of flavin in NQO by a 19% decrease in absorption intensity at the 461 nm peak and a redshift of 8 nm at both peaks. Initial QM/MM calculations with NQO demonstrated that deprotonating Y277 in the absence of solution ions alters the absorption spectrum of flavin by decreasing the intensity at the 461 nm peak, increasing the intensity at the 368 nm peak, and red shifting both peaks. The predictions made by the QM/MM calculations were tested in solution, where the effect of unprotonated Y277 on flavin’s absorption spectrum was masked by adding NaCl to a solution containing NQO at pH 11.5. It is important to note that the QM/MM calculations probed the effect of forming unprotonated Y277 while the biochemical experiment probed the effect of masking unprotonated Y277; thus, the results between the two techniques are consistent when the observations are qualitatively opposite. The results of the computational and biochemical experiments consistently determined deprotonating Y277 decreases the intensity of the 461 nm peak and redshifts both flavin peaks; however, the experiments were not qualitatively consistent at the 368 nm peak. The unexpected increase in flavin’s absorption intensity at the 368 nm peak in solution may be due to a conformational change that occurs in NQO following the addition of NaCl. Alternatively, it is possible the addition of NaCl alters the environment surrounding the

flavin by perturbing other active site ionizable residues instead of only masking unprotonated Y277. Elucidating the unexpected increase in intensity at the 368 nm peak following the addition of NaCl to NQO at pH 11.5 will be the subject of future studies. Here, we describe how the negative point charge on Y277 can modify the spectroscopic properties of oxidized flavin to provide biochemists with a better understanding of how proteins can modulate flavins as a spectroscopic probe.

3.5 Materials and Methods

3.5.1 Materials

QIAprep Spin Miniprep Kit was purchased from Qiagen (Valencia, CA). Isopropyl-1-thiol-β-D-galactopyranoside (IPTG) was ordered from Promega (Madison, WI). *Escherichia coli* strains DH5α and Rosetta(DE3)pLysS were purchased from Invitrogen Life Technologies (Grand Island, NY) and Novagen (Madison, WI), respectively. HiTrapTM Chelating HP 5 mL affinity column and prepacked PD-10 desalting columns were purchased from GE Healthcare (Piscataway, NJ). Riboflavin 5' Phosphate Sodium Salt was purchased from MP Biomedicals LLC (Solon, OH). All other reagents used were of the highest purity commercially available.

3.5.2 Enzyme Preparation

The synthesis and cloning of the gene for NQO variant Y277F in a pET20b(+) plasmid was prepared by Genescript (Piscataway, NJ). Upon delivery, the mutant gene was sequenced by Macrogen Inc. (Rockville, MD). Plasmids were purified using the Qiagen QIAquick Spin Miniprep Kit according to the manufacturer's protocol. Resulting purified plasmids were transformed into chemically competent *E. coli* strain Rosetta(DE3)pLysS cells using the heat shock method.[67] NQO-Y277F was expressed in *E. coli* strain Rosetta(DE3)pLysS and purified through methods previously described for NQO-WT.[33] Purified NQO-Y277F was stored at −20

°C in 20 mM NaP_i, pH 8.0, 100 mM NaCl, and 10% glycerol. The protocol was adjusted so that the storage buffer contained NaP_i instead of TRIS-HCl, and the concentration of NaCl was reduced to 100 mM, to improve the stability of NQO-Y277F in storage and solution. The total protein concentration was determined using the Bradford method.[68]

3.5.3 UV-Visible Absorption Spectroscopy

UV-visible absorption spectra were recorded using an Agilent Technologies model HP 8453 PC diode-array spectrophotometer (Santa Clara, CA) equipped with a thermostated water bath. For the pH dependence on the UV-visible absorption spectra of flavin, buffers were exchanged with 10 mM NaP_i, 10 mM NaP_iP_i, pH 8.0, 100 mM NaCl, and 20% glycerol, using a PD-10 desalting column. The UV-visible absorption spectra of NQO-WT, NQO-Y277F, and free-FMN were measured as a function of pH at 15 °C. Each 2.5-mL buffered solution was subjected to 1-10 μL serial additions of 1 M NaOH using a 10 μL syringe while the solution was stirring. Absorption spectra were incrementally taken in the pH range from 8.0 to 11.5. After each addition of base, the system was allowed to equilibrate until no changes in the pH value and absorbance were observed, which typically required 1-2 min. The resulting spectra were corrected for absorbance at 800 nm and the incremental dilution factor by NaOH addition. For enzyme solutions, the spectra were corrected for concentration using ε_{461} = 12,400 $M^{-1}cm^{-1}$ for NQO-WT[33] and ε_{461} = 12,000 $M^{-1}cm^{-1}$ for NQO-Y277F (this study). The extinction coefficient of NQO-Y277F was determined by extracting the flavin cofactor by heat denaturation in 20 mM KP_i, pH 7.0, and 200 mM NaCl at 25 ° C.[69]

The effect of adding NaCl on the UV-visible absorption spectra of NQO-WT at pH 11.5, NQO-WT at pH 9.5, and free-FMN were determined. NQO-WT was prepared in a 50 mM piperidine solution, at pH 9.5 or 11.5, using a PD-10 desalting column, while free-FMN was

prepared in 10 mM HEPES at pH 8.0. After collecting 1 mL of each solution, an absorption spectrum was immediately taken at 10 °C with air blowing towards the cuvette to prevent moisture condensation. Following the initial spectrum, NaCl was added to a final concentration of 100 mM, and a spectrum was taken 2 min after the addition to allow the solution to equilibrate. For NQO-WT at pH 11.5, the absorption spectrum took an hour to equilibrate.

3.5.4 Steady-State Kinetics

Enzymatic activity was measured using an Agilent Technologies model HP 8453 PC diode-array spectrophotometer equipped with a thermostated water bath. The steady-state kinetic parameters for NQO-WT and NQO-Y277F were measured using the method of initial rates where the concentrations of NADH and benzoquinone were varied from 25-100 μM and 10-200 μM, respectively.[70] Stock solutions of benzoquinone were prepared in 100% ethanol. The effect of ethanol on enzyme activity was minimized by ensuring the final concentration of ethanol in the assay reaction mixture was at 1%. The assay was run in 20 mM KP_i, pH 7.0, and 100 mM NaCl at 25 °C. Reaction rates were measured by following NADH consumption at 340 nm using ε_{340} = 6,220 $M^{-1}cm^{-1}$.[71] For each point, the reaction between NADH and benzoquinone was measured as a baseline before the addition of enzyme at a final concentration of 100 nM.

3.5.5 Data Analysis

All data were fit using KaleidaGraph software (Synergy Software, Reading, PA). The effect of pH on the UV-visible absorption spectra of NQO-WT and NQO-Y277F was fit to Eq 1, which describes a curve with one pK_a value and two limiting values at high pH (A) and low pH (B). The kinetic data determined from initial rates using varying concentrations of NADH and benzoquinone was fit to Eq 2, which describes a ping-pong bi-bi steady-state kinetic mechanism with no inhibition by either substrate; here, v_0 represents the initial rate of reaction, e is the

concentration of enzyme, k_{cat} is the maximum rate of enzyme turnover at saturating concentrations of both NADH and benzoquinone, and K_{NADH} and K_{BQ} are the Michaelis constants for NADH and benzoquinone, respectively.

$$Y = \frac{A+B\times10^{(pK_a-pH)}}{1+10^{(pK_a-pH)}} \quad (1)$$

$$\frac{v_0}{e} = \frac{k_{cat}[NADH][BQ]}{K_{NADH}[BQ]+K_{BQ}[NADH]+[NADH][BQ]} \quad (2)$$

3.5.6 Density Functional Theory Model Calculations

ESTMs (E_1 and E_2 **Fig. 3.2**) were computed for lumiflavin, a minimal flavin model, in ref. 32 at the B3LYP/6-31+G* level of theory. Note, however, that the colors here are inverted with respect to refs. *25*, *32* since the maps presented here indicate the effect of a negative charge on the absorption wavelength of each band (instead of a positive charge as reported in refs. *25*, *32*). The oscillator strength tuning maps were computed using the exact same protocol,[32] but instead of plotting the surface maps as a function of the excitation energy, the maps are generated using the computed oscillator strength as a function of external charge position on the van der Waals surface of lumiflavin.

To support the result of the tuning map calculations, another model calculation was performed with a B3LYP/6-31+G* geometry-optimized lumiflavin model and a tyrosine point charge model placed at the same position and orientation relative to flavin as in the crystallographic crystal structure of NQO. The TD-B3LYP/6-31+G* oscillator strength of lumiflavin was computed in the presence of the tyrosine, which was described using amber99sb point charges.[72] The calculation was then repeated in the presence of tyrosinate. The calculation in the presence of the tyrosinate had a 20% smaller oscillator f_1 and a 47% larger f_2, in qualitative agreement with the trend expected from the tuning maps.

3.5.7 Quantum Mechanical/Molecular Mechanical (QM/MM) Calculations

The QM/MM calculations of NQO-WT and NQO-Y277F were performed using the Average Solvent Electrostatic Configuration – Free Energy Gradient (ASEC-FEG) protocol. The ASEC-FEG approach combines the idea of the Average Solvent Electrostatic Configuration model,[52, 53] originally developed to study molecular systems in solution, and the Free Energy Gradient method proposed by Nagaoka *et al*.[54, 56, 57] ASEC-FEG has been extended to proteins by including van der Waals average interaction energy,[58] and has recently been extended to model flavoproteins.[55]

Briefly, ASEC-FEG is an approach that computes QM/MM energies and properties in a superposition of several protein configurations sampled by molecular dynamics instead of using one single representative structure. The protein is divided into two subsystems: (i) the QM subsystem, comprising the lumiflavin shown in Fig. 3.8, and (ii) The MM region, which includes all other atoms in the simulation (the ribose-5′-phosphate group, the protein, the solvent, and

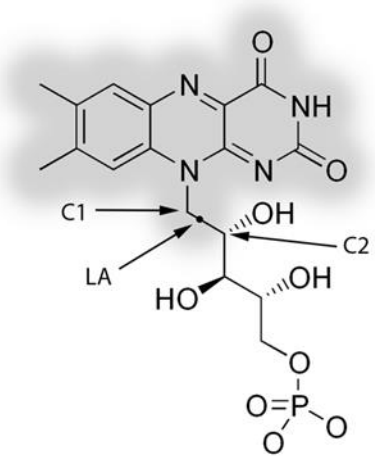

Figure 3.8. The QM/MM Frontier Region.
The lumiflavin (shaded region) is treated at the quantum mechanical (QM) level of theory, while the ribose-5'-phosphate group, the protein, and solvent as described using molecular mechanics (MM) force fields.

solution ions). The frontier between the QM and the MM parts is treated using the link atom (LA) approach.[73] The LA position is restrained according to the Morokuma scheme.[74]

To locate stationary structures (e.g., minima) of the QM subsystem on the free energy surface of the protein, the average forces acting on each atom of the QM subsystem is calculated using the free energy gradient obtained through the following approximation:

$$F(q) = -\frac{\partial G(q)}{\partial q} = -\left\langle \frac{\partial V}{\partial q} \right\rangle \approx -\frac{\partial \langle V \rangle}{\partial q} \qquad (3)$$

In this equation, q represents the nuclear coordinates of the QM subsystem, G is the free energy of the system, and V is the potential energy of the QM subsystem, including the interaction energy with the rest of the protein. These forces are equal to the time-averaged forces acting on each atom of the QM subsystem over the equilibrium distribution of the total system, as obtained from a molecular dynamics (MD) simulation.

The potential energy of the system in Eq. 4 is decomposed in the following way:

$$V = V_{\mathrm{QM}} + V_{\mathrm{QM/MM}} \qquad (4)$$

V_{QM} represents the potential energy of the QM atoms, while $V_{\mathrm{QM/MM}}$ is the interaction energy between the QM and MM subsystems. This term includes several components:

$$V_{\mathrm{QM/MM}} = V_{\mathrm{ele}}(QM/MM) + V_{\mathrm{vdw}}(QM/MM) + V_{\mathrm{bond}}(QM/MM) \qquad (5)$$

The first interaction term is the electrostatic interaction energy between the QM atoms and the MM atoms of the system. This term is considered in this work through the ElectroStatic Potential Fitted (ESPF) method.[75, 76] V_{vdw} (QM/MM) represents the van der Waals interaction energy between the QM atoms and the MM atoms of the system, where van der Waals parameters are assigned both to the QM and to the MM atoms. The last term of Eq. 5 deals with an empirical bonded interaction between the QM and MM atoms at the frontier.

The ASEC configuration in this context is an ensemble of protein configurations that provide a time-averaged MM environment interaction with the QM subsystem. 100 protein configurations included in the ASEC environment are selected at regular time intervals from a 500 ns molecular dynamics simulation. The charge and van der Waals parameters of these 100 configurations are scaled by 0.01 to generate the MM field acting on the QM subsystem.

The QM/ASEC configuration is used as a starting point to perform a QM/MM geometry optimization of the QM subsystem in the field of the ASEC environment. Two steps, generation of the APEC configuration around a fixed QM subsystem and QM/ MM geometry optimization in a fixed ASEC environment, are repeated iteratively until the energy difference relative to the previous step is less than a threshold of 0.5 kcal/mol. The geometry and ESPF charges of the QM subsystem are updated in each cycle.

The details of the molecular dynamics simulations are as follows: The NQO-WT and NQO-Y277F were solvated in a 70 Å cubic water box. The molecular dynamics simulations were carried out using the GROMACS code[77] with AMBER99sb[72] and TIP3P[78] force fields for the protein and water molecules, respectively. An initial pre-equilibration of the entire system was performed in the NPT ensemble, heating the system from 0 to 300 K in 300 ps, followed by 1000 ps of equilibration. The MD is then performed in the NVT ensemble using 5000 ps for thermalization and 500 ns for production under standard room conditions. Periodic boundary conditions (PBC) were used to avoid boundary effects. In order to neutralize the total negative charge of some of these proteins, Cl^- ions were added to the solvent box using the "genion" procedure implemented in the GROMACS.

To study the effect of solution ions, in addition to the Cl^- ions needed to neutralize the system, 18 pairs of Na^+ and Cl^- ions (1 NaCl per 555 water molecules, equivalent to a ca. 100 mM

NaCl solution) were added to the solvent box, and molecular dynamics simulations were repeated using the same conditions.

The details of the QM/MM calculations are as follows: The link atom is used to separate the lumiflavin, which is neutral, from the ribose-5′-phosphate group, which is parametrized to have a total charge of -2. The MM atom closest to the link atom (**Fig. 3.8**) has its charge set to zero to avoid over-polarizing the QM/MM frontier. The QM subsystem is treated at complete-active-space self-consistent field (CASSCF) level of theory[79] and using the ANO-L-VDZP basis set.[80] The active space used is 16 electrons and 14 orbitals, which includes all the π-electron systems, excluding one π and π* orbital. The ASEC configuration used in the QM calculations comprises all the atoms within 30 Å from the flavin molecule. This selection is assumed to be a better compromise than using a cubic system to avoid nonsymmetric effects. The QM subsystem is optimized in the field of the 30 Å ASEC configuration. The final optimized structure is used to compute the oscillator strength and excitation energy of the system. The spectral shifts were computed using the multiconfigurational complete active space second-order perturbation theory (CASPT2)[81] with the ANO-L-VDZP basis set to account for a substantial part of the dynamical correlation energy. The oscillator strength values were computed both at the DFT (B3LYP/aug-cc-pVDZ) level of theory. All the multiconfigurational calculations were computed by using the MOLCAS-TINKER interface,[82, 83] while the DFT were computed in Gaussian 03.[84]

3.6 References

[1] Dickey, A., and Faller, R. (2008) Examining the contributions of lipid shape and headgroup charge on bilayer behavior, *Biophys. J. 95*, 2636-2646.

[2] Lee, A. G. (2004) How lipids affect the activities of integral membrane proteins, *Biochim. Biophys. Acta 1666*, 62-87.

[3] Tyauble, H., Teubner, M., Woolley, P., and Eibl, H. (1976) Electrostatic interactions at charged lipid membranes. I. Effects of pH and univalent cations on membrane structure, *Biophys. Chem. 4*, 319-342.

[4] Barroso da Silva, F. L., Derreumaux, P., and Pasquali, S. (2018) Protein-RNA complexation driven by the charge regulation mechanism, *Biochem. Biophys. Res. Commun. 498*, 264-273.

[5] Draper, D. E. (2004) A guide to ions and RNA structure, *RNA 10*, 335-343.

[6] Lipfert, J., Doniach, S., Das, R., and Herschlag, D. (2014) Understanding nucleic acid-ion interactions, *Annu. Rev. Biochem. 83*, 813-841.

[7] Owczarzy, R., You, Y., Moreira, B. G., Manthey, J. A., Huang, L., Behlke, M. A., and Walder, J. A. (2004) Effects of Sodium Ions on DNA Duplex Oligomers: Improved Predictions of Melting Temperatures, *Biochemistry 43*, 3537-3554.

[8] Gadda, G. (2012) Oxygen Activation in Flavoprotein Oxidases: The Importance of Being Positive, *Biochemistry 51*, 2662-2669.

[9] Garcia-Viloca, M., Gao, J., Karplus, M., and Truhlar, D. G. (2004) How enzymes work: analysis by modern rate theory and computer simulations, *Science 303*, 186-195.

[10] Gitlin, I., Carbeck, J. D., and Whitesides, G. M. (2006) Why are proteins charged? Networks of charge-charge interactions in proteins measured by charge ladders and capillary electrophoresis, *Angew. Chem. Int. Ed. Engl. 45*, 3022-3060.

[11] Harris, T. K., and Turner, G. J. (2002) Structural Basis of Perturbed pKa Values of Catalytic Groups in Enzyme Active Sites, *IUBMB Life 53*, 85-98.

[12] Roth, J. P., and Klinman, J. P. (2003) Catalysis of electron transfer during activation of O2 by the flavoprotein glucose oxidase, *Proc. Nat. Acad. Sci. U.S.A. 100*, 62.

[13] Schwans, J. P., Sunden, F., Gonzalez, A., Tsai, Y., and Herschlag, D. (2013) Uncovering the determinants of a highly perturbed tyrosine pKa in the active site of ketosteroid isomerase, *Biochemistry 52*, 7840-7855.

[14] Liu, Y., Thoden, J. B., Kim, J., Berger, E., Gulick, A. M., Ruzicka, F. J., Holden, H. M., and Frey, P. A. (1997) Mechanistic Roles of Tyrosine 149 and Serine 124 in UDP-galactose 4-Epimerase from Escherichia coli, *Biochemistry 36*, 10675-10684.

[15] Gribenko, A. V., and Makhatadze, G. I. (2007) Role of the Charge–Charge Interactions in Defining Stability and Halophilicity of the CspB Proteins, *J. Mol. Biol. 366*, 842-856.

[16] Gribenko, A. V., Patel, M. M., Liu, J., McCallum, S. A., Wang, C., and Makhatadze, G. I. (2009) Rational stabilization of enzymes by computational redesign of surface charge–charge interactions, *Proc. Nat. Acad. Sci. U.S.A. 106*, 2601.

[17] Sanchez-Ruiz, J. M., and Makhatadze, G. I. (2001) To charge or not to charge?, *Trends Biotechnol. 19*, 132-135.

[18] Feig, M., and Pettitt, B. M. (1999) Sodium and Chlorine Ions as Part of the DNA Solvation Shell, *Biophy. J. 77*, 1769-1781.

[19] Maffeo, C., Yoo, J., Comer, J., Wells, D. B., Luan, B., and Aksimentiev, A. (2014) Close encounters with DNA, *J. Phys. Condens. Matter 26*, 413101-413101.

[20] Hud, N. V., and Plavec, J. (2003) A unified model for the origin of DNA sequence-directed curvature, *Biopolymers 69*, 144-158.

[21] Rubinstein, A., and Sherman, S. (2004) Influence of the solvent structure on the electrostatic interactions in proteins, *Biophys. J. 87*, 1544-1557.

[22] Suliman, M. A., El Tinay, A. H., Elkhalifa, A., Babiker, E. E., and Elkhalil, E. A. (2006) Solubility as influenced by pH and NaCl concentration and functional properties of lentil proteins isolate, *Pakistan J. Nutr. 5*, 589-593.

[23] Xiong, Y. L., Lou, X., Wang, C., Moody, W. G., and Harmon, R. J. (2000) Protein Extraction From Chicken Myofibrils Irrigated with Various Polyphosphate and NaCl Solutions, *J. Food Sci. 65*, 96-100.

[24] Su, D., Aguillon, C., and Gadda, G. (2019) Characterization of conserved active site residues in class I nitronate monooxygenase, *Arch. Biochem. Biophys. 672*, 108058.

[25] Kabir, M. P., Orozco-Gonzalez, Y., and Gozem, S. (2019) Electronic spectra of flavin in different redox and protonation states: a computational perspective on the effect of the electrostatic environment, *Phys. Chem. Chem. Phys. 21*, 16526-16537.

[26] Ghisla, S., Massey, V., Lhoste, J. M., and Mayhew, S. G. (1974) Fluorescence and optical characteristics of reduced flavines and flavoproteins, *Biochemistry 13*, 589-597.

[27] Draper, R. D., and Ingraham, L. L. (1968) A potentiometric study of the flavin semiquinone equilibrium, *Arch. Biochem. Biophys. 125*, 802-808.

[28] Macheroux, P. (1999) UV-Visible Spectroscopy as a Tool to Study Flavoproteins, In *Flavoprotein Protocols* (Chapman, S. K., and Reid, G. A., Eds.), pp 1-7, Humana Press, Totowa, NJ.

[29] Macheroux, P., Kappes, B., and Ealick, S. E. (2011) Flavogenomics – a genomic and structural view of flavin-dependent proteins, *FEBS J. 278*, 2625-2634.

[30] Kotaki, A., Naoi, M., Okuda, J. U. N., and Yagi, K. (1967) Absorption and Fluorescence Spectra of Riboflavin Tetrabutyrate in Various Solvents, *J. Biochem. 61*, 404-406.

[31] Massey, V., and Ganther, H. (1965) On the interpretation of the absorption spectra of flavoproteins with special reference to D-amino acid oxidase, *Biochemistry 4*, 1161-1173.

[32] Orozco-Gonzalez, Y., Kabir, M. P., and Gozem, S. (2019) Electrostatic Spectral Tuning Maps for Biological Chromophores, *J. Phys. Chem. B 123*, 4813-4824.

[33] Ball, J., Salvi, F., and Gadda, G. (2016) Functional Annotation of a Presumed Nitronate Monoxygenase Reveals a New Class of NADH:Quinone Reductases, *J. Biol. Chem. 291*, 21160-21170.

[34] Deller, S., Macheroux, P., and Sollner, S. (2007) Flavin-dependent quinone reductases, *Cell. Mol. Life Sci. 65*, 141.

[35] Iyanagi, T., and Yamazaki, I. (1970) One-electron-transfer reactions in biochemical systems V. Difference in the mechanism of quinone reduction by the NADH dehydrogenase and the NAD(P)H dehydrogenase (DT-diaphorase), *Biochim. Biophys. Acta Bioenerg. 216*, 282-294.

[36] Brunmark, A., and Cadenas, E. (1989) Redox and addition chemistry of quinoid compounds and its biological implications, *Free Rad. Biol. Med. 7*, 435-477.

[37] Ezraty, B., Gennaris, A., Barras, F., and Collet, J.-F. (2017) Oxidative stress, protein damage and repair in bacteria, *Nat. Rev. Microbiol.15*, 385.

[38] Patridge, E. V., and Ferry, J. G. (2006) WrbA from *Escherichia coli* and *Archaeoglobus fulgidus* Is an NAD(P)H:Quinone Oxidoreductase, *J. Bacteriol. 188*, 3498.

[39] Wang, G., and Maier, R. J. (2004) An NADPH Quinone Reductase of *Helicobacter pylori* Plays an Important Role in Oxidative Stress Resistance and Host Colonization, *Infect. Immun. 72*, 1391.

[40] Brock, B. J., and Gold, M. H. (1996) 1,4-Benzoquinone Reductase from the BasidiomycetePhanerochaete chrysosporium:Spectral and Kinetic Analysis, *Arch. Biochem. Biophys. 331*, 31-40.

[41] Sollner, S., Nebauer, R., Ehammer, H., Prem, A., Deller, S., Palfey, B. A., Daum, G., and Macheroux, P. (2007) Lot6p from Saccharomyces cerevisiae is a FMN-dependent reductase with a potential role in quinone detoxification, *FEBS J. 274*, 1328-1339.

[42] Laskowski, M. J., Dreher, K. A., Gehring, M. A., Abel, S., Gensler, A. L., and Sussex, I. M. (2002) FQR1, a Novel Primary Auxin-Response Gene, Encodes a Flavin Mononucleotide-Binding Quinone Reductase, *Plant Physiol. 128*, 578.

[43] Sparla, F., Tedeschi, G., and Trost, P. (1996) NAD(P)H:(Quinone-Acceptor) Oxidoreductase of Tobacco Leaves Is a Flavin Mononucleotide-Containing Flavoenzyme, *Plant Physiol. 112*, 249.

[44] Bianchet, M. A., Faig, M., and Amzel, L. M. (2004) Structure and Mechanism of NAD[P]H:Quinone Acceptor Oxidoreductases (NQO), In *Methods Enzymol.*, pp 144-174, Academic Press.

[45] Harada, S., Fujii, C., Hayashi, A., and Ohkoshi, N. (2001) An Association between Idiopathic Parkinson's Disease and Polymorphisms of Phase II Detoxification Enzymes:

Glutathione S-Transferase M1 and Quinone Oxidoreductase 1 and 2, *Biochem. Biophys. Res. Comm. 288*, 887-892.

[46] Ball, J., Reis, R. A. G., Agniswamy, J., Weber, I. T., and Gadda, G. (2019) Steric hindrance controls pyridine nucleotide specificity of a flavin-dependent NADH:quinone oxidoreductase, *Protein Sci. 28*, 167-175.

[47] Latovitzki, N., Halper, J. P., and Beychok, S. (1971) Spectrophotometric titration of tyrosine residues in human lysozyme, *J. Biol. Chem. 246*, 1457-1460.

[48] Macheroux, P., Massey, V., Thiele, D. J., and Volokita, M. (1991) Expression of spinach glycolate oxidase in Saccharomyces cerevisiae: purification and characterization, *Biochemistry 30*, 4612-4619.

[49] Meyer, T. E., Bartsch, R. G., Caffrey, M. S., and Cusanovich, M. A. (1991) Redox potentials of flavocytochromes c from the phototrophic bacteria, Chromatium vinosum and Chlorobium thiosulfatophilum, *Arch. Biochem. Biophys. 287*, 128-134.

[50] Stenberg, K., Clausen, T., Lindqvist, Y., and Macheroux, P. (1995) Involvement of Tyr24 and Trp108 in substrate binding and substrate specificity of glycolate oxidase, *Eur. J. Biochem. 228*, 408-416.

[51] Jeffrey, G. A., and Jeffrey, G. A. (1997) *An introduction to hydrogen bonding*, Vol. 12, Oxford university press New York.

[52] Canuto, S. (2010) *Solvation effects on molecules and biomolecules: computational methods and applications*, Vol. 6, Springer Science & Business Media.

[53] Coutinho, K., Georg, H. C., Fonseca, T. L., Ludwig, V., and Canuto, S. (2007) An efficient statistically converged average configuration for solvent effects, *Chem. Phys. Lett. 437*, 148-152.

[54] Hirao, H., Nagae, Y., and Nagaoka, M. (2001) Transition-state optimization by the free energy gradient method: Application to aqueous-phase Menshutkin reaction between ammonia and methyl chloride, *Chem. Phys. Lett. 348*, 350-356.

[55] Iyer, A., Reis, R. A. G., Gannavaram, S., Momin, M., Spring-Connell, A. M., Orozco-Gonzalez, Y., Agniswamy, J., Hamelberg, D., Weber, I. T., Gozem, S., Wang, S., Germann, M. W., and Gadda, G. (2021) A Single-Point Mutation in d-Arginine Dehydrogenase Unlocks a Transient Conformational State Resulting in Altered Cofactor Reactivity, *Biochemistry 60*, 711-724.

[56] Okuyama-Yoshida, N., Kataoka, K., Nagaoka, M., and Yamabe, T. (2000) Structure optimization via free energy gradient method: Application to glycine zwitterion in aqueous solution, *J. Chem. Phys. 113*, 3519-3524.

[57] Okuyama-Yoshida, N., Nagaoka, M., and Yamabe, T. (1998) Transition-state optimization on free energy surface: Toward solution chemical reaction ergodography, *Int. J. Quantum Chem. 70*, 95-103.

[58] Orozco-Gonzalez, Y., Manathunga, M., Marin, M. D. C., Agathangelou, D., Jung, K. H., Melaccio, F., Ferre, N., Haacke, S., Coutinho, K., Canuto, S., and Olivucci, M. (2017) An Average Solvent Electrostatic Configuration Protocol for QM/MM Free Energy Optimization: Implementation and Application to Rhodopsin Systems, *J. Chem. Theory Comput. 13*, 6391-6404.

[59] Hückel, E., and Debye, P. (1923) The theory of electrolytes: I. lowering of freezing point and related phenomena, *Phys. Z 24*, 1.

[60] Kumar, S., and Nussinov, R. (2002) Close-range electrostatic interactions in proteins, *Chem. Bio. Chem. 3*, 604-617.

[61] Kumar, S., and Nussinov, R. (2002) Relationship between ion pair geometries and electrostatic strengths in proteins, *Biophys. J. 83*, 1595-1612.

[62] Warshel, A., Russell, S. T., and Churg, A. K. (1984) Macroscopic models for studies of electrostatic interactions in proteins: limitations and applicability, *Proc. Natl. Acad. Sci. U.S.A. 81*, 4785-4789.

[63] Gavish, N., and Promislow, K. (2016) Dependence of the dielectric constant of electrolyte solutions on ionic concentration: A microfield approach, *Phys. Rev. E 94*, 012611.

[64] Kontogeorgis, G. M., Maribo-Mogensen, B., and Thomsen, K. (2018) The Debye-Hückel theory and its importance in modeling electrolyte solutions, *Fluid Ph. Equilibria 462*, 130-152.

[65] Levy, A., Andelman, D., and Orland, H. (2012) Dielectric constant of ionic solutions: a field-theory approach, *Phys. Rev. Lett. 108*, 227801.

[66] Olivares, W., and McQuarrie, D. A. (1975) On the theory of ionic solutions, *Biophys. J. 15*, 143-162.

[67] Inoue, H., Nojima, H., and Okayama, H. (1990) High efficiency transformation of Escherichia coli with plasmids, *Gene 96*, 23-28.

[68] Bradford, M. M. (1976) A rapid and sensitive method for the quantitation of microgram quantities of protein utilizing the principle of protein-dye binding, *Anal. Biochem. 72*, 248-254.

[69] Whitby, L. G. (1953) A new method for preparing flavin-adenine dinucleotide, *Biochem. 54*, 437-442.

[70] Allison, D., and Purich, D. L. (1979) Practical considerations in the design of initial velocity enzyme rate assays.

[71] Horecker, B., and Kornberg, A. (1948) The extinction coefficients of the reduced band of pyridine nucleotides, *J. Biol. Chem. 175 1*, 385-390.

[72] Hornak, V., Abel, R., Okur, A., Strockbine, B., Roitberg, A., and Simmerling, C. (2006) Comparison of multiple Amber force fields and development of improved protein backbone parameters, *Proteins 65*, 712-725.

[73] Singh, U. C., and Kollman, P. A. (1986) A combined ab initio quantum mechanical and molecular mechanical method for carrying out simulations on complex molecular systems: Applications to the CH3Cl+ Cl− exchange reaction and gas phase protonation of polyethers, *J. Comput. Chem. 7*, 718-730.

[74] Humbel, S., Sieber, S., and Morokuma, K. (1996) The IMOMO method: Integration of different levels of molecular orbital approximations for geometry optimization of large systems: Test for n-butane conformation and SN 2 reaction: RCl+ Cl−, *J. Chem. Phys. 105*, 1959-1967.

[75] Ferré, N., and Ángyán, J. G. (2002) Approximate electrostatic interaction operator for QM/MM calculations, *Chem. Phys. Lett. 356*, 331-339.

[76] Melaccio, F., Olivucci, M., Lindh, R., and Ferré, N. (2011) Unique QM/MM potential energy surface exploration using microiterations, *Int. J. Quantum Chem.111*, 3339-3346.

[77] Abraham, M. J., Murtola, T., Schulz, R., Páll, S., Smith, J. C., Hess, B., and Lindahl, E. (2015) GROMACS: High performance molecular simulations through multi-level parallelism from laptops to supercomputers, *SoftwareX 1*, 19-25.

[78] Jorgensen, W. L., Chandrasekhar, J., Madura, J. D., Impey, R. W., and Klein, M. L. (1983) Comparison of simple potential functions for simulating liquid water, *J. Chem. Phys. 79*, 926-935.

[79] Roos, B. O., Taylor, P. R., and Sigbahn, P. E. M. (1980) A complete active space SCF method (CASSCF) using a density matrix formulated super-CI approach, *Chem. Phys. 48*, 157-173.

[80] Widmark, P.-O., Malmqvist, P.-Å., and Roos, B. O. (1990) Density matrix averaged atomic natural orbital (ANO) basis sets for correlated molecular wave functions, *Theor. Chima. Acta 77*, 291-306.

[81] Andersson, K., Malmqvist, P. A., Roos, B. O., Sadlej, A. J., and Wolinski, K. (1990) Second-order perturbation theory with a CASSCF reference function, *J. Chem. Phys. 94*, 5483-5488.

[82] Aquilante, F., Autschbach, J., Carlson, R. K., Chibotaru, L. F., Delcey, M. G., De Vico, L., Fdez. Galván, I., Ferré, N., Frutos, L. M., and Gagliardi, L. (2016) Molcas 8: New capabilities for multiconfigurational quantum chemical calculations across the periodic table, Wiley Online Library.

[83] Ponder, J. W., and Case, D. A. (2003) Force fields for protein simulations, *Adv. Protein Chem. 66*, 27-85.

[84] Frisch, M. J., Trucks, G. W., Schlegel, H. B., Scuseria, G. E., Robb, M. A., Cheeseman, J. R., Scalmani, G., Barone, V., Petersson, G. A., Nakatsuji, H., Li, X., Caricato, M., Marenich, A. V., Bloino, J., Janesko, B. G., Gomperts, R., Mennucci, B., Hratchian, H. P., Ortiz, J. V., Izmaylov, A. F., Sonnenberg, J. L., Williams, Ding, F., Lipparini, F., Egidi, F., Goings, J., Peng, B., Petrone, A., Henderson, T., Ranasinghe, D., Zakrzewski, V. G., Gao, J., Rega, N., Zheng, G., Liang, W., Hada, M., Ehara, M., Toyota, K., Fukuda, R., Hasegawa, J., Ishida, M., Nakajima, T., Honda, Y., Kitao, O., Nakai, H., Vreven, T., Throssell, K., Montgomery Jr., J. A., Peralta, J. E., Ogliaro, F., Bearpark, M. J., Heyd, J. J., Brothers, E. N., Kudin, K. N., Staroverov, V. N., Keith,

T. A., Kobayashi, R., Normand, J., Raghavachari, K., Rendell, A. P., Burant, J. C., Iyengar, S. S., Tomasi, J., Cossi, M., Millam, J. M., Klene, M., Adamo, C., Cammi, R., Ochterski, J. W., Martin, R. L., Morokuma, K., Farkas, O., Foresman, J. B., and Fox, D. J. (2016) Gaussian 16 Rev. C.01, Wallingford, CT.

4 CONCLUSION

In this thesis, NQO was utilized to study the roles of two non-catalytic residues located in the 'activity' subunit of the TIM-barrel domain through a combination of UV-visible absorption spectroscopy, molecular dynamics, and steady-state kinetics. In the first portion of this thesis, the conserved residue P78 was replaced with glycine to study the significance of gate rigidity on the ability of NQO to form the enzyme-substrate complex. Molecular dynamic simulations of NQO-P78G and NQO-WT with NAD^+ bound and in the ligand-free forms demonstrated the mutant enzyme samples wider conformations of the gate in the ligand-free form of NQO, without affecting the dynamics of the enzyme-substrate complex. Despite the altered gate dynamics of NQO-P78G, a comparison of the steady-state kinetic parameters between the mutant and wild-type enzymes demonstrated replacement of P78 with glycine resulted in a minimal increase in the rate of substrate association with the oxidizing substrate. However, the slight increase in the rate of substrate association is of interest as mutations at conserved residues typically decrease the enzymatic efficiency of enzymes. The *de novo* synthesis of enzymes commonly utilizes multiple mutations to reengineer catalytic functions; thus, in combination with other point mutations, the P78G mutation may support an increase in the rate of substrate association by destabilizing the dynamics of the gate in NQO.

An analysis of the crystal structures of NQO demonstrated the hydroxyl O atom of Y277 is distanced 3.0 Å from the C_7 methyl group of the FMN cofactor, suggesting the active site residue may be utilized as a model system to elucidate the relationship between flavin’s absorption spectrum and active site environment. In the second part of this thesis, UV-visible absorption spectroscopy with NQO-WT and NQO-Y277F was used to establish Y277 deprotonates to form a tyrosinate at high pH. An investigation on the relationship between unprotonated Y277 and flavin's

absorption properties was pursued to assess how the active site environment of NQO can modulate the flavin cofactor's spectral features. A combination of UV-visible absorption spectroscopy and QM/MM computations demonstrated anionic Y277 can decrease the intensity of 461 nm peak and redshift both peaks in the flavin's absorption spectrum; however, when the biochemical and computational techniques included solution ions, the observed effect was masked. QM/MM calculations probed the distribution of solution ions in NQO, which revealed either the Na^+ ions move closer to the protein surface and/or the Cl^- ions move away from the protein surface following Y277 deprotonation. Interestingly, the results presented here demonstrate the environment surrounding the protein can modulate the negative charge of unprotonated Y277 on flavin's absorption properties through a long-range counterion effect reminiscent of an “ionic atmosphere”.

In summary, the results presented in this thesis demonstrate that mutating P78G widens the dynamics of the gate in NQO to expose the active site of the enzyme to the bulk solvent. Furthermore, deprotonating Y277 observed a unique interaction between an active site point charge and the solution ions. Although neither P78 nor Y277 play a key role in the turnover of NQO, the current investigation elucidates the significance of the non-catalytic residues in the ‘activity’ subunit of a TIM-barrel fold by demonstrating a P78G mutation alters gate dynamics and Y277 deprotonation in the absence of solution ions can modulate flavin absorption properties in NQO.